Journal of Structural Geology, Vol. 9, No. 5/6, pp. 747 to 778, 1987
Printed in Great Britain

0191-8141/87 $03.00 + 0.00

Special Research Paper*

Simple shear experiments on calcite rocks: rheology and microfabric

S. M. SCHMID,† R. PANOZZO† and S. BAUER‡

†Geologisches Institut, ETH-Zentrum, 8092 Zürich, Switzerland and ‡Center for Tectonophysics, Texas A & M University, College Station, Texas 77843. Now at: Sandia National Laboratories, Div. 6314, Albuquerque, NM 87185, U.S.A.

(*Received* 20 *June* 1986; *accepted in revised form* 26 *February* 1987)

Abstract—Ideal simple shearing of Carrara marble and Solnhofen limestone was achieved by inserting calcite rock slices into sandstone cylinders precut at 35°. The experiments covered a wide range in temperatures (25–900°C) at confining pressures of 200 and 250 MPa and at strain rates between 10^{-3} and 10^{-5} s^{-1}. Shear strains of up to $\gamma = 2.7$ were achieved. The stress–strain data for simple shear favourably compare with predictions on the basis of existing flow laws established in coaxial testing. This comparison demonstrates that the simple shear experiments covered most of the previously established flow regimes for calcite rocks. At the highest temperatures Carrara marble exhibited substantial work softening after high shear strains. A complete texture analysis was carried out with the U-stage and a texture goniometer. The following four distinct microfabric regimes were found. (1) *Twinning regime*: an oblique *c*-axis maximum deflected from the pole to the flattening plane towards σ_1 and against the imposed sense of shear results directly from *e*-twinning. Extensive twinning (some grains are completely twinned) rapidly rotates the *c*-axes into near parallelism with σ_1. This regime was observed for Carrara marble deformed at temperatures below 700°C and for Solnhofen limestone at room temperature. (2) *Intracrystalline slip regime*: three *c*-axis maxima were observed in both rock types at more elevated temperatures and in the absence of twinning. These *c*-axis orientations result from an alignment of slip planes and slip directions into parallelism with the shear-zone boundary and the shear direction, respectively. This finding supports the idea of an 'orientation for easy slip' resulting from simple shearing. In addition to *r*- and *f*-glide, basal glide is inferred to have been operative. (3) *Grain-boundary sliding regime*: a great circle distribution of *c*-axes approximately perpendicular to the direction of finite shortening is observed. This texture is weaker compared to the other regimes. It is interpreted to result from minor contributions of *f*-slip towards total strain. This regime is restricted to fine-grained Solnhofen limestone deformed at the highest temperatures. (4) *Grain-boundary migration regime*: only in Carrara marble deformed at the highest temperatures is there substantial grain-boundary migration recrystallization. The texture consists of a dominant *c*-axis maximum oriented perpendicular to the shear-zone boundary. This single maximum corresponds to an 'orientation for easy slip' for basal slip. Grain-boundary migration assists rapid lattice reorientation, and leads to (geometrical) work softening. Quantitative analysis of grain-boundary surface orientations gave the following results. Within the twinning and the intracrystalline slip regimes the characteristic grain shape is elliptical for both rock types. The strain ellipses derived from this analysis closely correspond to the known finite strain at the lowest temperatures. At intermediate temperatures, and especially in Carrara marble, there is a consistent trend for the aspect ratios to indicate too little flattening, and for the angles between the long axis of the strain ellipse and the shear-zone boundary to be too small. In the absence of grain boundary migration recrystallization this finding indicates minor translations of grains with respect to one another (grain-boundary sliding or translations accommodated in the mantle regions of grains). At the highest temperatures, where extensive grain-boundary migration occurs in Carrara marble (grain-boundary migration regime), two preferred orientations of grain boundaries are observed: (1) parallel to the shear zone boundary; and (2) parallel to an oblique direction deflected 20° away from the normal to the shear-zone boundary in the sense of the imposed shear. The same pattern of grain-boundary alignment is observed in Solnhofen limestone deformed in the grain-boundary sliding regime. The geological applications of this experimental work are discussed in terms of calcite tectonites in particular and sheared rocks in general.

INTRODUCTION

CLASSICAL rock deformation experiments are usually performed in coaxial deformation and under conditions deviating from plane strain (uniaxial compression or extension). In view of the fact that rock deformation under natural conditions commonly involves a strong component of non-coaxial (or rotational) deformation and often fairly closely approximates conditions of plane strain it seems appropriate to attempt simple shear deformation in the laboratory in spite of the additional technical difficulties.

The principal aims of this study are: (1) to compare rheological behaviour and microfabric development in simple shear with earlier results obtained by coaxial testing of the same starting material; (2) to improve our understanding of the microfabric development under conditions of simple shear, both in terms of the development of grain shapes (microstructure) and the mechanisms of the development of a crystallographic preferred orientation (referred to as 'texture' in this study); and (3) to provide useful criteria for detecting rotational deformation, including information on the shear sense, for microfabric studies on naturally deformed rocks.

The two calcite rocks (Solnhofen limestone and Carrara marble) were chosen because a great number of

*This special long paper was accepted on its exceptional scientific merit.

data are already available from coaxial testing of the same or similar materials (e.g. Casey *et al.* 1978, Rutter 1974, Schmid *et al.* 1977, 1980), and because the flow strength of calcite is low enough to permit simple shearing with the experimental procedure chosen for this study. However, many of the results will be of general interest in regard to other rock-forming minerals, especially in regard to texture development under conditions of simple shear.

A small number of studies with similar aims have been carried out in the past. Rutter & Rusbridge (1977), Friedman & Higgs (1981) and Kern & Wenk (1983) also used calcite rocks, and Bouchez & Duval (1982) performed simple shear deformation with ice. Rutter & Rusbridge (1977) approximated simple shear by the application of two increments of pure shear at different angles. Friedman & Higgs (1981) deformed calcite gouge under conditions of temperature and strain rates which are similar to the ones used in our experiments and their experimental procedure is identical to the one used in this study. In fact, they inspired one of us to carry out more experiments. The main shortcoming of their pioneering work is that a cohesionless gouge rather than a slab of intact rock was used, Thus, the microfabric of their starting material is fairly complex and differs significantly from the microfabric of intact calcite rock. There was a large range in grain size, large amounts of elastic energy were stored in the crystals due to the grinding process, and compaction and sintering must have occurred during the experiment. Kern & Wenk (1983) used a very complex experimental assembly which only approximated simple shear and covered a small range in temperature and strain rate.

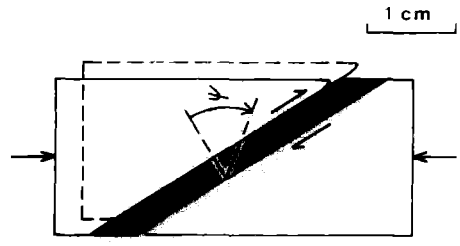

Fig. 1. Sketch of the experimental assembly consisting of two half-cylinders of Tennessee sandstone (white) and a wafer of solid rock (Solnhofen limestone or Carrara marble, black) deformed in simple shear. The shear angle ψ is a function of wafer thickness and axial displacement.

APPARATUS AND TECHNIQUE

Cylindrical specimens of Tennessee sandstone (4 cm long with a diameter of 1.73 cm) were precut at an angle of 32° to the cylinder axis. The acute angle of the half-cylinders was rounded off in order to avoid puncture of the copper jacket during the sliding motion of the half-cylinders during testing. Wafers of Solnhofen limestone (grain size 4 μm) and Carrara marble (grain size 200 μm) were cut from a cylinder at the same 32° angle and sandwiched between the sandstone driving blocks (Fig. 1). The thickness of the wafers was chosen to be 1 mm or 2.7 mm (see Table 1). The assembly was wrapped in copper foil in order to fit tightly in the copper jacket.

The complete assembly was then mounted into a triaxial apparatus described by Friedman *et al.* (1979) and deformed under conditions of strain rate and temperature listed in Table 1. The apparatus is internally

Table 1. Experimental data on Solnhofen limestone (ST) and Carrara marble (CT) specimens

Specimen	Temp. (°C)	Shear strain rate (s^{-1})	Confining pressure (MPa)	Shear stress (MPa)	Thickness shear zone (mm)	Permanent shear (γ)	Microfabric regime
ST 6	25	4.7 E-4	250	269.2 *	2.84	1.09	TW
ST 2	500	5.0 E-4	250	149.0 †	2.79	1.22	ICS
ST 1	700	1.0 E-3	250	70.0 †	2.74	1.07	ICS
ST 5	700 ‡	5.1 E-4	200	41.0 §	2.67	0.92	GBS
ST 7	800	3.2 E-4	200	6.2	2.79	1.13	GBS
		9.4 E-4		11.9			
		1.9 E-4		4.4			
		9.8 E-4		13.2			
		3.2 E-4		7.0			
ST 4	900	5.1 E-4	200	6.0 §	2.55	1.36	GBS
CT 9	350	4.2 E-4	200	140.0 ‖	1.06	1.27	TW
CT 5	500	5.0 E-4	200	128.5 ‖	2.73	1.08	TW
CT 1	600	1.0 E-3	250	81.0 ‖	2.74	1.22	TW
CT 6	700	4.7 E-4	200	72.2 *	0.97	2.85	ICS
CT 3	700	2.8 E-5	200	52.7 *	2.69	0.79	ICS
CT 2	800	1.0 E-3	200	39.2 *	2.64	0.63	GBM
CT 7	800	1.3 E-4	200	39.2 *	1.02	2.74	GBM
CT 4	900	4.9 E-4	200	25.4 *	2.74	1.31	GBM

* Ultimate strength.
† Steady state stress.
‡ Bad temperature control (±50°C).
§ Stress at γ = 0.22.
‖ Stress at γ = 0.5.

TW Twinning.
ICS Intracrystalline slip.
GBS Grain-boundary sliding.
GBM Grain-boundary migration.

heated and uses argon as a confining medium. The load is measured externally.

Shearing of the inserted calcite rock was achieved by choosing a confining pressure (200 or 250 MPa) high enough to elevate frictional resistance along the cohesionless interface between the calcite specimen and sandstone well above the flow resistance within the calcite layer. As a consequence, the sandwiched calcite wafer deformed by ductile simple shear. Microstructural investigations confirmed that no discrete slip occurred along the sandstone–calcite interface. The thickness of the wafers was measured before and after the experiment and no change in thickness was observed. Hence, the specimens were deformed under ideal simple shear conditions.

The total absence of flattening perpendicular to the shear zone is surprising at first sight. However, it is readily explained by the fact that the undeformable sandstone exerts a severe frictional restraint against viscous flow parallel to the sandstone–calcite interface necessary for extrusion of the calcite material between the sandstone half-cylinders. This restraint is highest in the immediate neighbourhood of the interface and the amount of extrusion is expected to depend on the aspect ratio of length to width of the calcite wafer. The wafers had a thickness of about 1 mm (for CT 6 and CT 7) and about 2.7 mm (for all the other experiments), whereas the length of the wafer measured along a medium cut through the assembly is about 30 mm. This high aspect ratio rendered extrusion, and hence shortening across the shear-zone boundary, impossible at the stress levels prevailing during simple shearing.

During the experiment axial displacement and axial load were monitored. The conversion into shear stress and shear strain with regard to the calcite wafer consisted of the following steps. Before mounting the specimen into the rig, the angles and exact dimensions of the pieces of the assembly were carefully measured for each individual run. The axial load was then first corrected for friction (external load measurement). Frictional resistance amounts to about 5000 N, corresponding to about 10 MPa shear stress on the shear-zone boundary of the assembly. Since friction certainly remained constant to within 10% during the run, the accuracy of the stress measurement can be given as ±0.5 MPa. Additionally the load measurement had to be corrected for copper strength and elastic bending of the sandstone driving-blocks and pistons. The latter factor is important and is caused by the sideways motion of the pistons as the sandstone driving-blocks slide past each other during simple shearing of the calcite wafer. The magnitude of this additional load correction was empirically calibrated. During some of the runs there was a leak in the copper jacket near the sandstone–calcite interface. This meant that the effective confining pressure was zero and that sliding along the cohesionless interface was entirely resisted by copper strength and elastic bending. Figure 2 shows that this correction amounts to about 6500 N axial load (equivalent to 13 MPa shear stress) at very large axial displacements (corresponding to $\gamma = 1$ and 3 for the thicker and thinner wafers, respectively). Thus, at high shear strains the accuracy of the stress measurement is further reduced by ±0.65 MPa, taking the calibration run to be reproducible to within 10%. Before calculating the shear stress from the corrected axial load another correction had to be applied to the contact area between wafer and driving blocks. Pressurization caused some slip to occur at the interfaces. Calibration runs determined the amount of area reduction to be 4 ± 0.9% of the nominal area. This introduces another uncertainty of ±0.9% of the calculated shear stress. In summary, the shear stresses given in Figs. 4 and 5 are accurate to within 0.5 and 1.2 MPa, depending on the shear strain, plus an additional 0.9% at any given stress level due to the contact area correction.

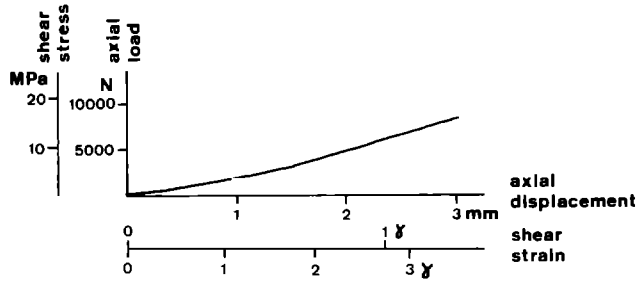

Fig. 2. Calibration curve of axial load vs axial displacement used for correcting copper strength and elastic bending of driving blocks and pistons. The corresponding stresses and shear strains resolved for the shear-zone boundary are also indicated. The equivalent γ-values refer to the thicker (top scale) and the thinner calcite wafers (bottom scale) used in the experiments.

For the calculation of the shear strain the axial displacements were first corrected for apparatus distortion. The finite shear strain values listed in Table 1 are permanent finite strains, i.e. the elastic contribution to the total finite strain was subtracted.

One of the great advantages of simple shear testing is the fact that very large strains can be achieved without running into severe problems of inhomogeneous strain within the specimen as is the case after about 20% shortening strain in coaxial testing. Inhomogeneous strains are restricted to a small region near the copper jacket, a region which was avoided in the microfabric analysis. Figure 3 graphically displays the shear strains γ equivalent to per cent shortening (engineering strain)

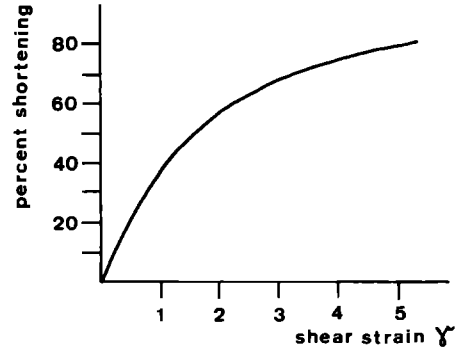

Fig. 3. Equivalent strain magnitudes of pure shear testing (per cent shortening) and simple shear testing (after Nadai 1963).

based on finding the following measure of strain magnitude e_m proposed by Nadai (1963):

$$e_m = 3^{-1/2}[(e_1 - e_2)^2 + (e_2 - e_3)^2 + (e_3 - e_1)^2]^{1/2}$$

where $e_{1,2,3}$ are the logarithmic strains. From this calculation it follows that a shear strain of $\gamma = 1$ corresponds to 37% shortening. Most experiments were carried out up to shear strains well in excess of $\gamma = 1$. The largest shear strain achieved was $\gamma = 2.85$, corresponding to 66% shortening.

STRESS–STRAIN DATA

The stress–strain curves

The shear stress vs shear strain curves of Figs. 4 and 5 cover a wide range of shear stresses due to the large temperature range of the experiments (for the exact experimental conditions, see Table 1). The results obtained on the two investigated rock types differ significantly, both in terms of strength and in the characteristics of the stress vs strain curves. This reflects differences in the deformation mechanisms due to the differences in initial grain size (4 and 200 μm for Solnhofen limestone and Carrara marble, respectively).

No strain softening was observed in the case of the runs on Solnhofen limestone (Fig. 4). The run at 25°C (ST 6) is characterized by a stress drop after the yield point, followed by strain hardening. Steady state flow was recorded at 500 and 700°C (ST 2 and ST 1). At 800 and 900°C (ST 7 and ST 4) or at 700°C and at lower strain rates (ST 5) some strain hardening is observed. This strain hardening is attributed to grain growth during the experiments causing an increase in strength due to a deformation mechanism sensitive to grain size. Rheological considerations and the fabric analysis suggest grain-boundary sliding. Schmid *et al.* (1977) also observed strain hardening due to grain growth in coaxial deformation and within this same flow regime (superplastic flow regime). Strain-rate stepping was performed with specimen ST 7 (800°C) in order to gain information on the strain-rate sensitivity of the flow stress described in the next sections.

The stress–strain curves for Carrara marble (Fig. 5) exhibit substantial amounts of work hardening up to 600°C. Within this temperature range twinning is an important deformation mechanism. This suggests that twinning is largely responsible for strain hardening. It will be shown later that twinning rapidly goes to completion within suitably oriented grains. As a consequence any further deformation has to be taken up by intracrystalline slip which has a higher critical resolved shear stress at low temperatures (Turner *et al.* 1954). Towards higher temperatures, work softening is observed. CT 6 (700°C) exhibits minor work softening after a shear strain of $\gamma = 1.2$. CT 7 (800°C) and CT 4 (900°C) feature substantial work softening after shear strains of $\gamma = 0.5$ and 0.15, respectively.

The stress–strain curves are very similar to those obtained in coaxial testing of the same materials (Rutter 1974, Schmid *et al.* 1977, 1980), both in terms of relative strength and as a function of strain rate and temperature. However, there is one important exception: no work softening was observed for Carrara marble under similar temperatures during coaxial testing (Schmid *et al.* 1980). Thus, the mechanism responsible for work softening obviously depends on the strain path.

A comparison of rheological data between coaxial and simple shear testing

Flow laws for both Solnhofen limestone and Carrara marble have been established over a wide range of

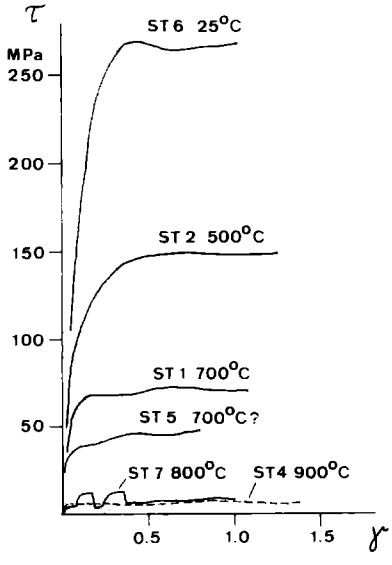

Fig. 4. Shear stress vs shear strain curves for Solnhofen limestone (for strain rates see Table 1). The curve for specimen ST 7 was obtained by changing the strain rate during the experiment.

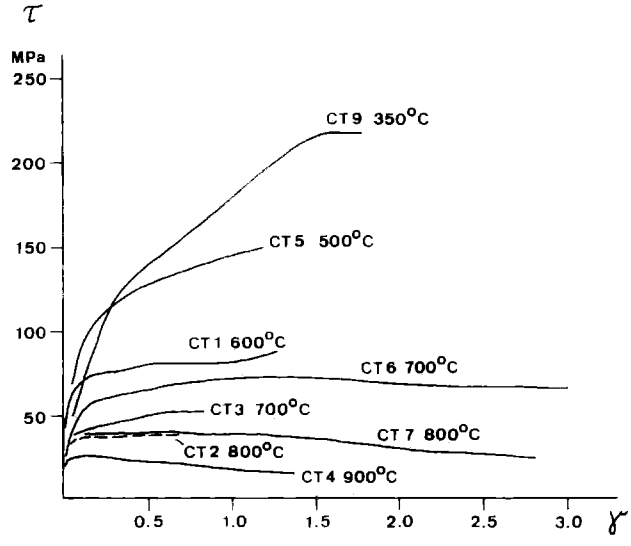

Fig. 5. Shear stress vs shear strain curves for Carrara marble (for strain rates see Table 1).

Table 2. The flow regimes in Solnhofen limestone and Carrara marble at temperatures above 400°C as defined by Schmid *et al.* (1977) and Schmid *et al.* (1980)

		Regime 1	Regime 2	Regime 3
Stress dependence	So	Exponential	Power law $n = 4.7$	Power law $n = 1.7$
	Ca	Exponential	Power law $n = 7.6$	Power law $n = 4.2$
Deformation mechanism	So	Dislocation glide	Dislocation creep	Grain-boundary sliding, superplasticity
	Ca	Dislocation glide, twinning	Dislocation creep, dynamic recrystallization	Dislocation creep, dynamic recrystallization

So: Solnhofen limestone.
Ca: Carrara limestone.

temperatures by conventional coaxial testing. Both rock types exhibit flow laws of the type

$$\dot{e} = A \exp (B \Delta\sigma) \quad (1)$$

up to temperatures of 500°C (Rutter 1974), where A is a pre-exponential constant incorporating the temperature dependence of strain rate, B a constant characterizing stress-dependence of strain rate and $\Delta\sigma$ the differential stress. Schmid *et al.* (1977, 1980) found that a power law of the form

$$\dot{e} = C(\Delta\sigma)^n \quad (2)$$

better describes the rheology at the higher temperatures. For both rock types three different flow regimes have been postulated (Schmid *et al.* 1977, 1980), and these are summarized in Table 2.

In order to compare pure shear with simple shear the flow laws obtained in pure shear (conventional testing) have to be generalized. The flow law relating shear strain rate to shear stress in simple shear can then be rederived from the generalized flow law.

In generalizing the flow laws of equations (1) and (2) we follow Nye (1953) who assumed: (1) that the third invariant of the deviatoric stress tensor is unimportant; and (2) that deformation does not change the volume of the material. As a consequence of these assumptions a generalized flow law can be formulated in terms of the second invariant of the deviatoric stress tensor, by analogy with the von Mises criterion used in plasticity.

For the case of simple shear, the flow laws can be derived from this generalized flow law (see Appendix 1). Expressed in terms of the constants A, B, C and n established by coaxial testing the flow laws valid for simple shear are:

$$\dot{\gamma}_{xy} = 2\,\dot{e}_{xy} = A\sqrt{3} \exp (B\sqrt{3}\,\tau_{xy}) \quad (3)$$

and

$$\dot{\gamma}_{xy} = 2\,\dot{e}_{xy} = C\,(\sqrt{3})^{n+1}(\tau_{xy})^n. \quad (4)$$

Figures 6 and 7 display in graphical form the flow laws obtained by equations (3) and (4) for the various temperatures used. The values of the constants A, B, C and n are taken from the flow laws published by Rutter (1974) and Schmid *et al.* (1977, 1980). The results of the simple shear tests are superimposed for comparison. In case of a work hardening the shear stresses were taken at a shear strain γ of 0.224 and 0.5, respectively (see Table 1). According to Fig. 3 these shear strains correspond to engineering strains of 10 and 20%, respectively. The flow laws established in coaxial testing refer to a stress level at 10% shortening. In view of the work hardening characteristics of the shear stress vs shear strain curves obtained for Carrara marble at low temperatures (Fig. 5) it seemed more appropriate to use the shear stress at $\gamma = 0.5$ (equivalent to 20% shortening) for comparison with the coaxial data.

The comparisons between predicted and measured strength (Figs. 6 and 7) show good agreement, particularly for the data on Carrara marble. Thus we conclude

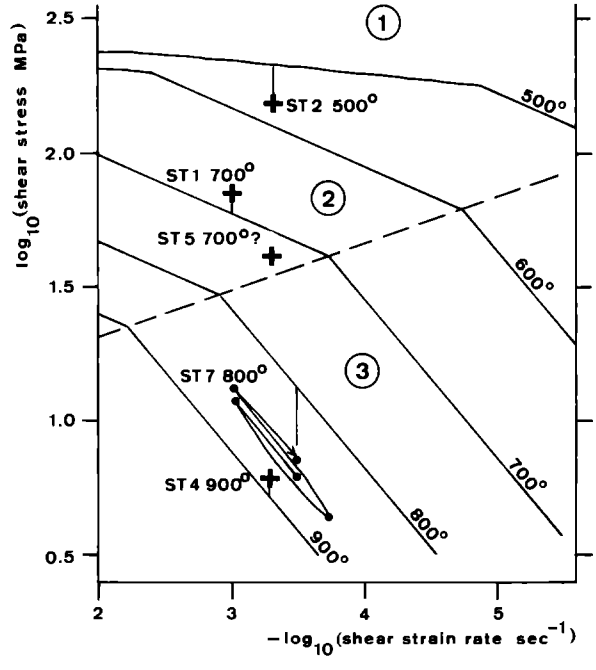

Fig. 6. Shear stress vs shear strain rate for Solnhofen limestone (log scale). Crosses indicate flow stresses recorded in the simple shear experiments. Best-fit lines correspond to predictions based on flow laws established in coaxial testing. Encircled numbers correspond to different flow regimes (compare Table 2) established by the work of Rutter (1974) and Schmid *et al.* (1977). Dashed line indicates the boundary between different flow regimes.

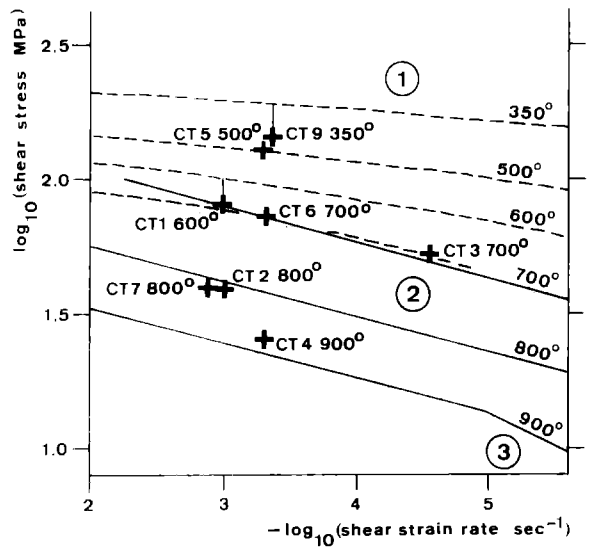

Fig. 7. Shear stress vs shear strain rate graph for Carrara marble (log scale) (see Fig. 6 caption). Best-fit curves were obtained from the flow laws established by Rutter (1974) in the case of flow regime 1 (dashed lines), and by Schmid *et al.* (1980) in the case of flow regimes 2 and 3 (solid lines).

that the assumptions behind generalizing flow laws according to Nye (1953) are justified and that the rheological behaviour observed in the simple shear experiments is compatible with the results from earlier work in coaxial testing.

Figures 6 and 7 now allow a prediction of the flow regime within which the simple shear experiments have been performed. In the following discussion it is important to note that flow regimes labelled '1', '2' and '3', as established for Solnhofen limestone (Schmid *et al.* 1977) and Carrara marble (Schmid *et al.* 1980) are not identical. Table 2 helps to clarify this somewhat unfortunate terminology.

Figure 6, featuring the Solnhofen limestone data, shows that ST 1, ST 2 and ST 5 are predicted to have been deformed in flow regimes 1 and 2, i.e. by dislocation glide and creep. ST 7 and ST 4 are predicted to have been deformed in flow regime 3, i.e. superplastically. The results of the strain-rate stepping experiments performed with ST 7 confirm that this specimen was deformed in a regime characterized by a power-law exponent $n < 3$, i.e. within the superplastic regime. The strength of ST 6 (25°C), deformed in a regime which is nearly strain-rate independent, is better predicted on the basis of the Mohr–Coulomb criterion. Taking the constants for the Mohr–Coulomb criterion determined for Solnhofen limestone at room temperature (Schmid 1975) a strength of $\Delta\sigma = 590$ MPa is calculated at 250 MPa confining pressure. Taking $\tau = \Delta\sigma/2$ (σ_1 is at 45° to the shear-zone boundary) a shear strength of 295 MPa is predicted, a value which compares well with the measured shear strength (268 MPa).

Figure 7 shows the Carrara marble data, and indicates that deformation by twinning (regime 1 for Carrara marble) is predicted for CT 5 and CT 9. CT 1, CT 6 and CT 3 were deformed in a transitional region between flow regimes 1 and 2. CT 2, CT 7 and CT 4 are predicted to have been deformed in flow regime 2 for Carrara marble (dislocation creep accompanied by dynamic recrystallization).

QUALITATIVE MICROSTRUCTURAL ANALYSIS AND TEXTURE ANALYSIS

Technique and data presentation

The texture analysis on selected Carrara marble specimens was carried out using the optical U-stage because the specimens were too coarse grained to be analysed by X-ray methods. In order to get optimal results the *c*-axis was determined with an accurate but tedious method proposed by Turner & Weiss (1963, p. 239). Instead of locating the fast vibration direction X directly, X was constructed as the pole to the great circle connecting a few individually measured Z (slow vibration) directions. In addition, the orientations of *e*-twin boundaries or lamellae ($01\bar{1}2$) and *r*-cleavage planes ($10\bar{1}1$) were measured in order to determine the complete crystal orientation for each grain. This complete texture analysis allowed the construction of pole figures for crystal directions other than *c* (0001).

The Solnhofen limestone specimens were analysed using the automatic X-ray texture goniometer installed at ETH Zürich. In order to obtain a surface large enough for reliable measurements (2.3 × 1.3 cm) the assembly pictured in Fig. 1 was cut parallel to the shear-zone boundary and through a median plane of the calcite wafer. Pole figures for eight different crystal directions were determined with the combined reflexion and transmission scan methods. The orientation distribution function (ODF) was calculated in order to obtain: (1) pole figures for particular crystal directions which cannot be measured (such as the slip direction common to *r*- and *f*-glide in calcite); (2) inverse pole figures for particular specimen directions; and (3) highly favoured crystal orientations. The co-ordinate system for the ODF representation was chosen such as to have specimen axes X_s, Y_s and Z_s parallel to the normal to the shear-zone boundary, the shear direction and the transverse direction, respectively. The crystal axes X_c, Y_c and Z_c are

Fig. 8. Photomicrographs of deformed Carrara marble (a)–(f) and Solnhofen limestone (g)–(h). The sense of shear is always dextral. (a) Specimen CT 1, deformed in the twinning regime at 600°C. Most grains show only one set of twins. (b) Specimen CT 5, deformed in the twinning regime at 500°C. Note slender triangular domains near grain boundaries representing relicts of the host grain. Within many grains twinning went to near-completion. (c) Specimen CT 6, deformed in the intracrystalline slip regime at 700°C. Extensive rotation recrystallization occurred in the grain-boundary region. Note the incipient development of a *C*-plane parallel to the shear-zone boundary (E–W-direction). (d) Detail of specimen CT 6, illustrating rotation recrystallization in the grain-boundary regions. The clearly visible narrow twin lamellae have probably been introduced during cooling and depressurization, and they accommodate only neglegible amounts of strain.

(*continued on p.* 755)

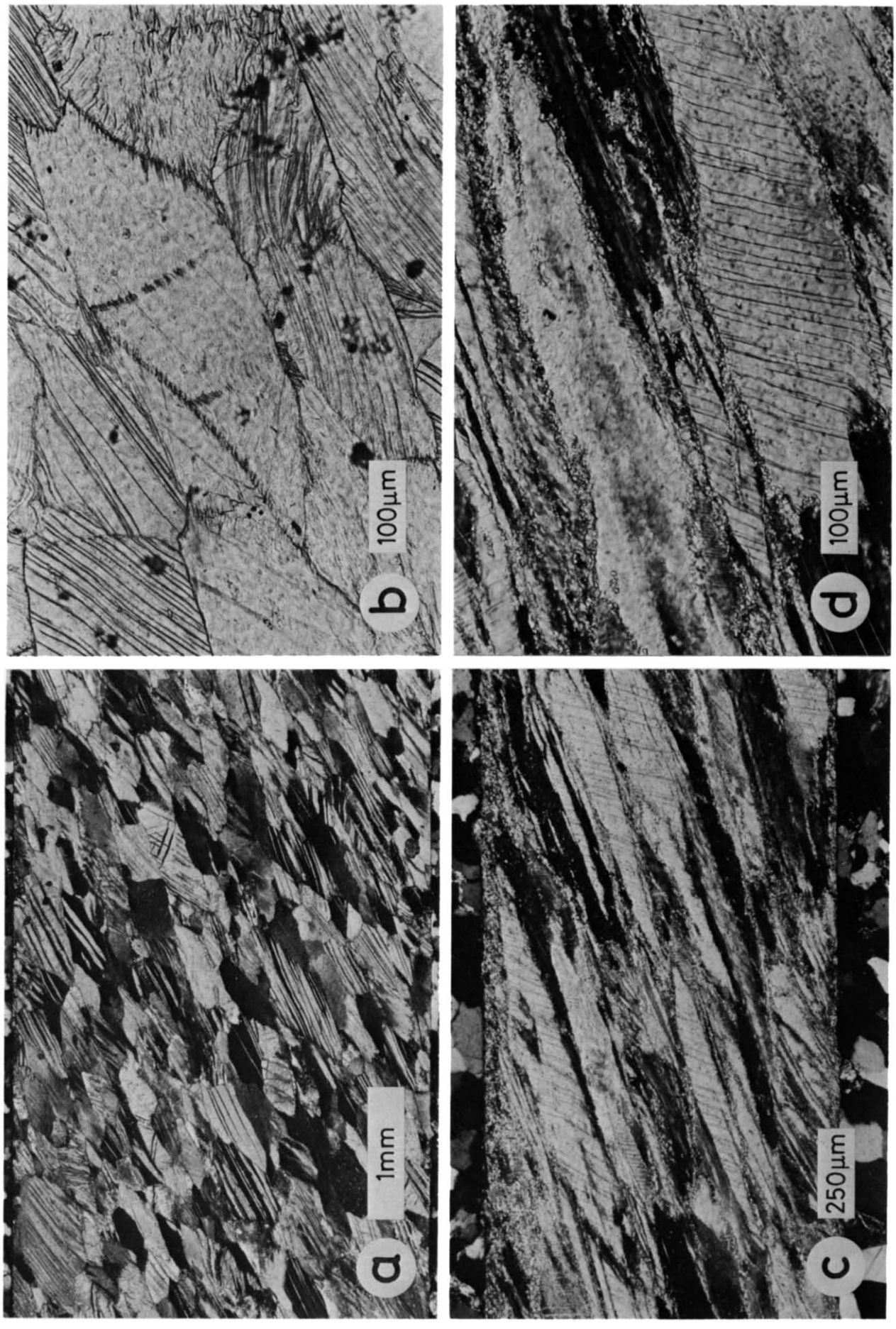

Fig. 8(a)–(d).

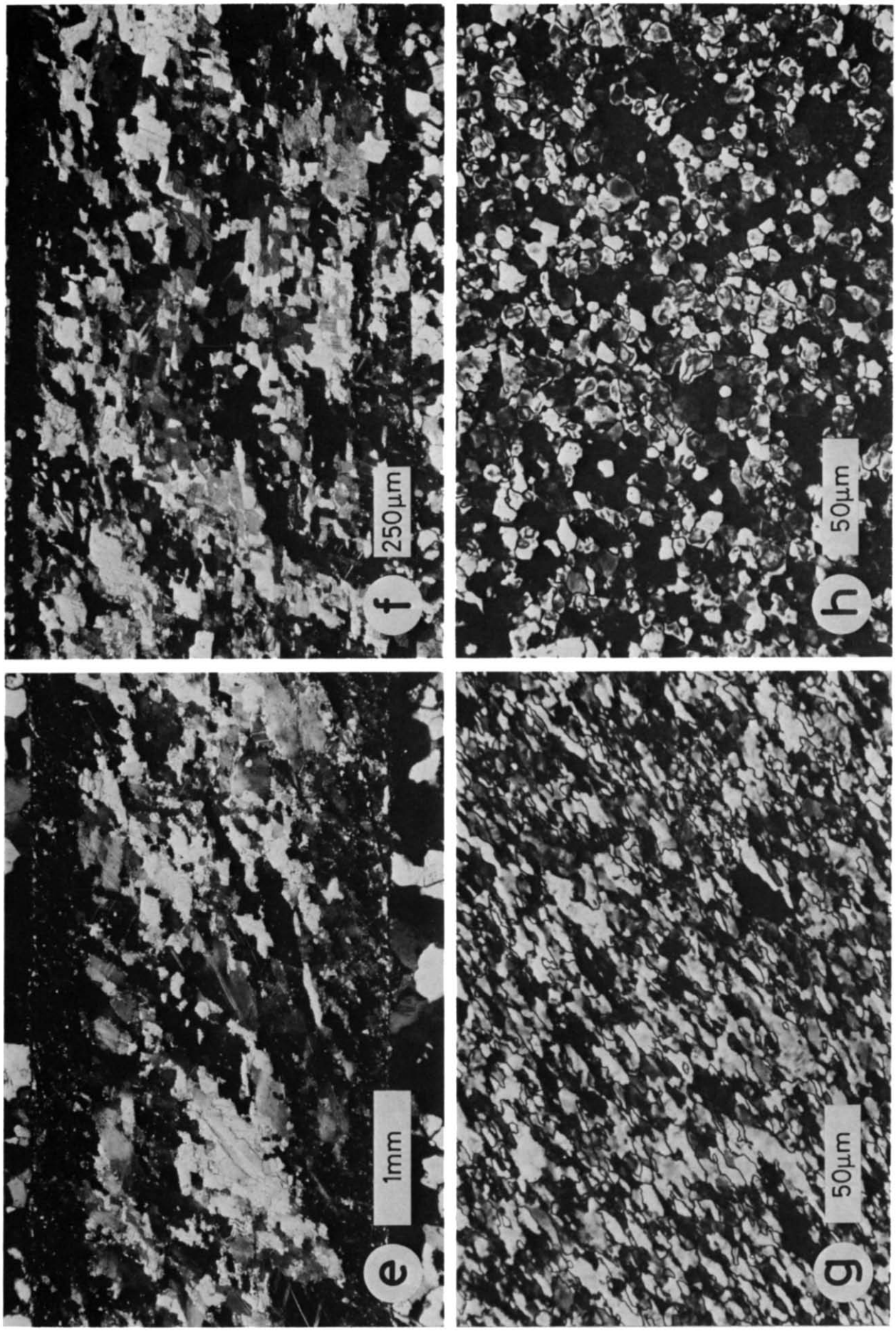

Fig. 8(e)–(h).

parallel to the *m*-, *a*- and *c*-axis directions, respectively. The Euler rotations were carried out according to Casey (1981, fig. 3). For more detail on the measuring and data processing procedure, as well as on the methods of data presentation the reader is referred to Bunge (1969), Casey (1981), Schmid *et al.* (1981) and Schmid & Casey (1986).

General remark concerning microfabric regimes

In the discussion of stress–strain data and flow laws the term 'flow regime' has been used in the previous sections and in earlier work on the rheology of calcite rocks. Each of these flow laws is valid for a certain range in deviatoric stress levels on the one hand, and a combination of temperature and strain rate on the other hand. These flow regimes reflect distinct deformation mechanisms whose exact nature is not always clear. Often, but not always, a flow regime is also characterized by a particular microstructure and texture. Because a direct correlation between: (1) deformation mechanism; (2) flow regime; and (3) the microfabric regime cannot always be made, it was decided to present the results of the microfabric analysis in terms of four distinct microfabric regimes. These microfabric regimes will be defined and described below purely on the basis of the observed characteristics in microstructure, and, in particular, the texture. Correlations with deformation mechanisms and flow regimes will be established.

THE TWINNING REGIME

Microstructural characteristics

Twin lamellae, and occasionally also a few deformation twins, are observed in all the specimens. Twin lamellae (i.e. very narrow twinned domains) are associated with negligible amounts of strain and may well have been initially present or formed during cooling and depressurizing. Deformation twins produced during the experiment are typically lensoid shaped with constricted ends at grain boundaries. An abundance of such twinned lenses characterizes what we refer to as the twinning regime (Fig. 8a & b).

Substantial amounts of deformation twins in Solnhofen limestone are only found in ST 6 deformed at room temperature. This is in agreement with the findings of Rutter (1970) that this rock does not twin any more at and above 400°C under laboratory conditions. Carrara marble deformed in the twinning regime at temperatures

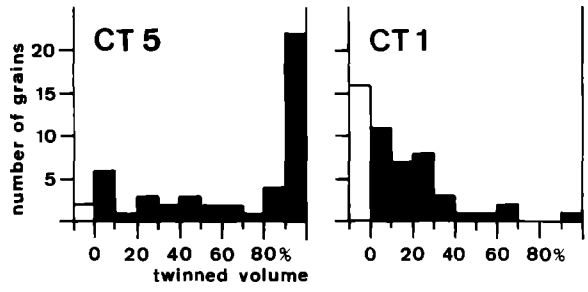

Fig. 9. Histograms indicating the fraction of crystal volume which is in a twinned orientation, obtained from a population of 50 neighbouring grains in specimens CT 5 (500°C) and CT 1 (600°C). White bar on left side: untwinned grains.

of 600°C and less and at shear stresses above 80 MPa (CT 9, CT 5 and CT 1). These findings agree with the predictions based on coaxial testing (Fig. 7) of the same material (flow regime 1 is identical with the twinning microfabric regime in the case of Carrara marble, see Table 2). In the simple shear experiments the vast majority of grains deformed by only one set of *e*-twins (Fig. 8a). This is in marked contrast to the coaxial tests on the same material where conjugate twins are frequently observed (Schmid *et al.* 1980). Although we are unable to find an obvious explanation for this finding, the observation of twinning on only one set of *e*-twins in naturally deformed rocks may give an indication for non-coaxial deformation.

In some of the grains within specimen CT 5 twinning went to completion within the grain interior. Only very narrow triangular domains along the grain boundaries remain in the untwinned orientation (Fig. 8b). In order to estimate the quantitative contribution of twinning to the total strain the volume fraction of the twinned domains was measured for a total of 50 neighbouring grains (under the U-stage, with the twin plane parallel to the viewing direction, and for the same population used for the texture analysis). The constriction of the twins at the grain boundaries made it easy to distinguish twinned and untwinned domains. The results of this analysis (Fig. 9) make it obvious that twinning is more important in CT 5, deformed within flow regime 1, as compared to CT 1, deformed in a transitional region between flow regimes 1 and 2 (see Fig. 6). The average volume fraction in a twinned orientation is 64% (CT 5) and 16% (CT 1). For crystallographic reasons total twinning would lead to a shear strain of $\gamma = 0.69$, under the simplifying assumption that the twin plane is oriented parallel to the shear-zone boundary. Consequently, the shear strains produced by twinning in CT 5 and CT 1

Fig. 8 *continued.* (e) Specimen CT 7, deformed in the grain-boundary migration regime at 800°C. Due to the higher shear strain, the preferred orientation is relatively strong compared to specimen CT 4 (f). Black grains have their *c*-axis normal to the shear-zone boundary. Recrystallization and degree of preferred orientation are most advanced in the neighbourhood of the driving blocks (dark rims). (f) Specimen CT 4, deformed in the grain-boundary migration regime at 900°C. Note the preferred alignment of grain boundaries along two sets of planes. One is aligned parallel to the shear zone boundary, the other at a high angle to the shear zone boundary. (g) Specimen ST 2, deformed in the intracrystalline slip regime at 500°C. Note the strong flattening of the grains and the serrate grain boundaries. (h) Specimen ST 4, deformed in the grain-boundary sliding regime at 900°C. Note the absence of flattening recorded by the grain shapes and the straight grain boundaries compared to ST 2 (g).

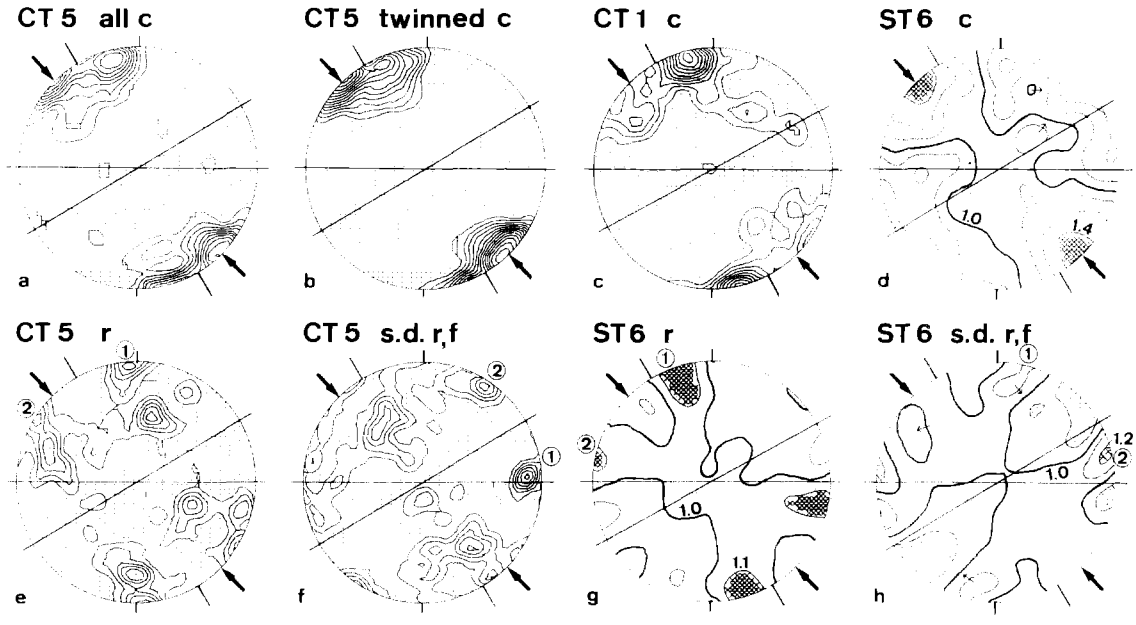

Fig. 10. Pole figures for specimens deformed in the twinning regime. This and all subsequent pole figures are equal-area projections, the EW-direction corresponds to the shear-zone boundary of the experiment and the sense of shear is dextral. Horizontal line: shear-zone boundary. Inclined line: plane of finite flattening. Pair of arrows: direction of σ_1. (a) All *c*-axes for CT 5 (500°C), twinned and untwinned domains. (b) *c*-axes of twinned domains only in CT 5. (c) All *c*-axes for CT 1 (600°C). (d) *c*-axis pole figure calculated from the ODF for ST 6 (25°C). (e), (g) Pole figures for the poles to the *r*-planes for CT 5 and ST 6, respectively. (f), (h) Pole figures for the slip direction, (s.d.), common to *r*- and *f*-planes ($r_1 : f_1$) = $(20\bar{2}1)$ for CT 5 and ST 6, respectively. Contours in multiples of a uniform distribution. Contour intervals 1.0 of a uniform distribution (a, b, c, e and f; optical data) and 0.1 of a uniform distribution (d, g and h; X-ray data, pole figures calculated from the ODF).

would be at most $\gamma = 0.44$ and 0.11, respectively. This is only a fraction of the total shear strains of $\gamma = 1.08$ and 1.22, respectively.

Texture analysis

The optically determined *c*-axis pole figures for Carrara marble exhibit a high-density area near the normal to the flattening plane with a tendency towards two sub-maxima (Fig. 10a & c). As seen from Fig. 11, which will be discussed in detail at a later stage, the active twin planes are oriented roughly parallel to the flattening plane. The single *c*-axis maximum obtained for Solnhofen limestone (ST 6) by using the X-ray method is deflected from the normal to the flattening plane in a direction towards the position of σ_1 (Fig. 10d). This sense of asymmetry has also been observed in natural calcite tectonites, which deformed in a shearing environment (Schmid *et al.* 1981, Dietrich & Song 1984). Note that the sense of deflection of the *c*-axis maximum is opposite to that observed in sheared quartz tectonites deformed by dislocation creep (Schmid & Casey 1986).

Mechanical twinning has been used to infer the direction of the principal compressive stress axis (e.g. Turner 1953, Dietrich & Song 1984, Spang 1974) and, additionally, for strain determinations (Groshong 1972). The diagrams of Fig. 11 (a & b) drawn after a procedure described by Dietrich & Song (1984) for two Carrara marble specimens deformed in the twinning regime, are very useful in discussing the validity of these methods and also for gaining insight into a mechanism of lattice reorientation peculiar to twinning. On this diagram the pole to the active *e*-twin plane is joined with the *c*-axis position of the host grain with the arrowhead pointing towards the *c*-axis of the host. Thus, the direction of the arrow indicates the shearing direction of the translation caused by twinning (see inset of Fig. 11).

The following points emerge from inspection of Fig. 11.

(1) Many twins operate in a shear sense which is opposite to the imposed shear sense.

(2) A substantial number of grains are twinned parallel to a direction pointing towards the center of the pole figure. This means that the intragranular deformation achieved by twinning strongly deviates from the plane strain conditions valid for the bulk strain in the aggregate.

From these findings we deduce that the twinning strain very strongly deviates from the bulk deformation of the specimens. A possible explanation for this behaviour is that the twins nucleate at the very early stages of the deformation path. Their initial orientation would be entirely controlled by the stress field. Also, the grains will suffer lattice rotations after large strains and the final orientation of the twins, as plotted in Fig. 11, will deviate from their original orientation. It was argued earlier that twinning only achieves a fraction of total strain and it is the additional activity of intracrystalline slip systems, such as glide on *r* or *f*, which will help to maintain strain compatibility between neighbouring grains.

Whereas twinning strain poorly reflects the imposed

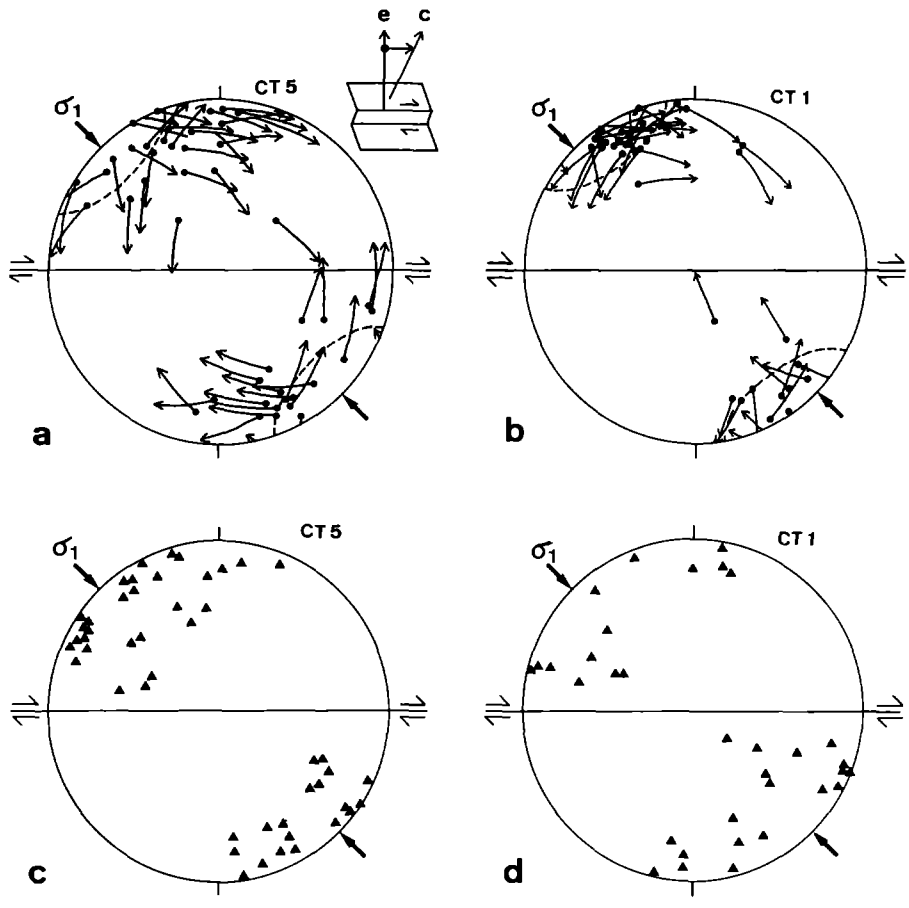

Fig. 11. Results of two methods for the determination of the direction of σ_1 applied to experimentally deformed material. (a) & (b): method proposed by Dietrich & Song (1984); (c) & (d) method proposed by Turner (1953). (a) & (b) The inset shows a section through a twinned calcite crystal illustrating that the arrow joining the pole to the active twin plane with the *c*-axis of the host grain indicates the direction of the translation caused by twinning (but not the amount in terms of the angle of shear). Arrowheads indicate the *c*-axis of the host, points indicate the pole to the active twin plane for the same grain. Direction and sense of the arrows correspond to the translation direction caused by twinning. The small circle with an opening angle of 26° is constructed (1) such as to contain a minimum number of host *c*-axis orientations (under conditions of homogeneous stress, grains with their *c*-axis within 26° to σ_1 cannot twin), and (2) with the arrows pointing away from the cone axis of the small circle. The cone axis corresponds to the inferred direction for σ_1; the actual position of σ_1 is indicated by arrows. (c) & (d) Triangles indicate the positions of σ_1 that would most effectively initiate twinning in each individual grain.

bulk strain it is a good indicator for the direction of the maximum compressive stress axis. We inferred the σ_1-direction with the method proposed by Dietrich & Song (1984) by finding the small circle representing a cone with an opening angle of 26° around σ_1, such that: (1) no *c*-axis positions for host grains are found within the small circle (twinning cannot operate for a direction of σ_1 which is within 26° from the *c*-axis of the host; and (2) the arrowheads (twinning direction) point away from the cone axis, i.e. σ_1. As shown in Fig. 11 the inferred σ_1-direction is very close to the known σ_1-direction at 45° from the shear-zone boundary, particularly for CT 5 (500°C, Fig. 11a). In the case of CT 1 (600°C, Fig. 11b) the strain achieved by twinning is very small and lattice rotations caused by intracrystalline slip may well be responsible for a noticeable deflection of the inferred σ_1 direction from the known position of σ_1. The comparison of Fig. 11(a) & (b) with Fig. 11(c) and (d), obtained by the classical method proposed by Turner (1953), shows that the new method proposed by Dietrich & Song (1984) locates the σ_1 position more accurately.

Before considering intracrystalline slip systems such as *r*-slip we first discuss the dramatic effect of twinning on the *c*-axis reorientation. Twinning rotates the *c*-axis of the twinned domain with respect to the *c*-axis position of the host grain in a direction towards σ_1, by an angle of 52°, and opposite to the sense of twinning translation. Thus, the main factor influencing lattice reorientation during twinning is the act of twinning, and not, as is the case in intracrystalline glide, compensatory rotations. By creating new crystal volume in a twinned orientation, the *c*-axis will rapidly move towards the direction of σ_1. This rotation of *c*-axes can be visualized by inspection of the arrows in Fig. 11(a) & (b): the *c*-axis of the twinned crystal domain is symmetrically disposed to the orientation of the host *c*-axis (arrow head) with respect to the *e*-poles. Thus, a large proportion of the *c*-axes of the twinned domains will come to lie within the 26° small circle around σ_1.

This reorientation is also illustrated in the *c*-axis pole figure for twinned domains only, obtained for specimen CT 5 (Fig. 10 b). The *c*-axis submaximum parallel to σ_1 is

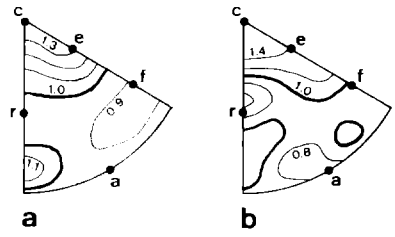

Fig. 12. Inverse pole figures. (a) Calculated from the ODF for specimen ST 6 (25°C), deformed in simple shear, and with respect to the specimen direction coinciding with the σ_1-direction during simple shear. Contour interval: 0.1 of a uniform distribution. (b) Calculated from a series of intensity profiles on a specimen of Solnhofen limestone, coaxially deformed at 20°C and up to 20% shortening (from Casey *et al.* 1978). Contour interval: 0.2 of a uniform distribution.

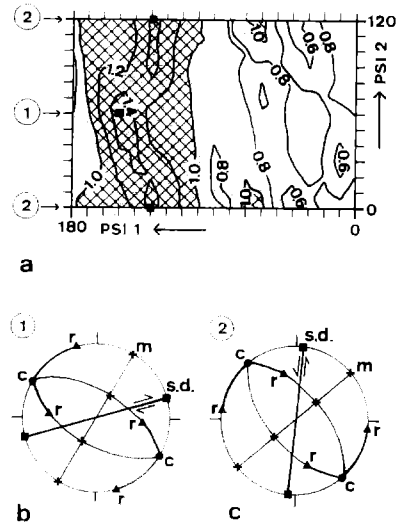

Fig. 13. Section through the graphical representation of the ODF and favoured crystal orientations, extracted from the ODF analysis for specimen ST 6 (25°C), deformed in the twinning regime. (a) Section at an angle of PHI = 90°. Contour intervals: 0.2 of a uniform distribution. Area with a density >1.0 cross-hatched. (b) & (c) Favoured crystal orientations corresponding to positions 1 and 2 in (a).

stronger than that in Fig. 10(a), which contains all *c*-axis orientations. Thus, the frequently observed obliquity of the *c*-axis maximum with respect to the flattening plane and in a sense towards σ_1 can be readily explained by lattice reorientation due to twinning.

Now we discuss the activity of intracrystalline slip systems with the help of selected pole figures (Fig. 10) and inverse pole figures (Fig. 12). The inverse pole figure for the direction of σ_1 obtained for ST 6 (Fig. 12a) is very similar to the inverse pole figure for the σ_1-direction as obtained from coaxial tests (Fig. 12b) carried out under similar conditions (Casey *et al.* 1978). Strictly, such a direct comparison should not be made because the specimens deformed in simple shear lack the axial symmetry observed for coaxially deformed specimens. Such a comparison is nevertheless useful because: (1) the shear strain $\gamma = 1.09$, applied to specimen ST 6, moves the direction of finite shortening away from σ_1 by an angle of only 14°; and (2) the calculation of an inverse pole figure for non-axially symmetric pole figure data artificially imposes a rotational symmetry with respect to the specimen direction considered. Nevertheless, the close similarity suggests that the mechanisms of lattice reorientation are the same for both specimens.

Inverse pole figures for coaxially deformed specimens with a maximum at *c* and a shoulder extending towards *e* have been observed by Wenk *et al.* (1973) and Casey *et al.* (1978) for specimens deformed in the twinning regime. Wenk *et al.* (1973) interpreted this texture to be caused by the simultaneous activity of *e*-twinning and duplex *r*-slip.

The pole figures for the poles to the *r*-planes (Fig. 10e & g) support the idea that *r*-slip is important in the case of simple shear as well. Two point concentrations of *r*-poles appear particularly clearly in Fig. 10(g). They correspond to two preferred orientations of *r*-planes, one in an orientation close to the shear-zone boundary (maximum 1 in Fig. 10e & g), and one at a high angle to the shear-zone boundary (maximum 2 in Fig. 10e & g). Slip along the *r*-planes corresponding to maximum 1 would be synthetic with the imposed shear sense, whereas slip along *r*-planes corresponding to maximum 2 would be antithetic. The slip direction contained in the preferred *r*-plane orientations appear at the margin of the pole figures plotted for the slip directions (Fig. 10f & h). Thus, both the orientations of slip planes and slip directions corresponding to maxima 1 and 2 are compatible with the plane strain simple shear conditions.

This interpretation is additionally supported by the analysis of the orientation distribution function obtained for specimen ST 6. Figure 13 features a section through the graphical representation of the ODF at an angle PHI = 90°. Following the convention of Eulerian angles as described by Casey (1981) this section graphically represents the favoured crystal orientations (i.e. the preferred orientation of crystal axes other than the *c*-axis) of all grains which have their *c*-axis at the periphery of the pole figure. The high intensity ridge shows a curved trace from a position at PSI 1 = 130°, PSI 2 = 0° (position 2 in Fig. 13a) through a position at PSI 1 = 150°, PSI 2 = 60° (position 1 in Fig. 13a), and back to position 2. The two ideal crystal orientations corresponding to positions 1 and 2 in Fig. 13(a) have been plotted in Fig. 13(b) & (c) where they are seen to correspond to the maxima 1 and 2 indicated in the pole figures of Fig. 10(e)–(h).

We thus conclude that the characteristic texture for the twinning regime may be interpreted to result from the following.

(1) A rapid reorientation of *c*-axes into a position near σ_1 due to the act of twinning.

(2) Deformation of the grains unsuitably oriented for twinning and further deformation of twinned grains by slip on two conjugate *r*-planes, both operating in a negative sense (following the convention of Turner & Weiss 1963).

It is interesting to note that for crystallographic reasons slip along an *r*-plane corresponding to position 1 (Fig. 10b) cannot take place within the same grain as slip along an *r*-plane corresponding to position 2 (Fig. 10c).

This suggests that strain due to *r*-slip and within an individual grain will strongly depart from the imposed bulk strain of the rock. A similar conclusion with regard to the twinning strains was already drawn from the analysis of twinning. These findings strongly support the idea of inhomogeneous strain on the scale of individual grains. A similar conclusion was drawn by Spiers (1979) for marble deformed in the twinning regime, and by Wenk *et al.* (1986) for fine-grained limestone.

THE INTRACRYSTALLINE SLIP REGIME

Microstructural characteristics

At lower flow stresses (i.e. at higher temperatures and/or lower strain rates) twinning is completely replaced by intracrystalline slip. This is in agreement with previous work on coaxial deformation of calcite rocks (Rutter 1974, Schmid *et al.* 1980, Schmid 1982a). The transition is readily explained by the results of the pioneering work on calcite single crystals by Turner *et al.* (1954). The critical resolved shear stress for *r*-slip is more strongly temperature dependent than that for *e*-twinning and hence *r*-slip completely replaces *e*-twinning at higher temperatures. Deformation bands and polygonization into subgrains are the optically visible traces of slip. In the case of Solnhofen limestone the originally serrate grain boundaries (compare fig. 6a in Schmid *et al.* 1977) remain serrate (Fig. 8g) and there are no signs of grain-boundary migration. Carrara marble often develops a core–mantle structure with subgrain formation in the grain-boundary region. After large strains (CT 6, Fig. 8c & d) recrystallization occurs preferentially in the grain boundary-region, and by progressive subgrain rotation. The recrystallized grains have a size of around 4 μm in this specimen deformed at a shear stress of 72 MPa. This grain size closely conforms to the stress vs recrystallized grain size relationship established by Schmid *et al.* (1980). Note that trails of recrystallized grains mark the site of incipient *C*-planes visible in specimen CT 6 (Fig. 8c). This indicates recrystallization induced strain softening (Schmid 1982b).

The transition from the twinning regime into the intracrystalline slip regime occurs at lower temperatures in Solnhofen limestone (<400°C) compared to Carrara marble (<700°C) at laboratory strain rates. This difference is caused by the difference in grain size (Schmid 1982a). Grain boundaries are serious obstacles to the propagation of broad deformation twins, and hence twinning competes more successfully with *r*-slip in coarse-grained calcite rocks. In terms of flow regimes this transition is identical with the transition from flow regime 1 into flow regime 2 for Carrara marble. In the case of Solnhofen limestone both flow regimes 1 and 2 produce a similar microstructure characterized by serrate grain boundaries and a clearly visible shape anisotropy of individual grains (Fig. 8g). Due to the small grain size, not much can be said about intragranular strain features in Solnhofen limestone.

Texture analysis

To a first approximation the *c*-axis pole figures for Solnhofen limestone specimens ST 2 and ST 1 (500 and 700°C, Fig. 14a & e) and Carrara marble specimen CT 6 (700°C, Fig. 15a) can be characterized by three point maxima located at the margin of the pole figure (labelled 1, 2 and 3 in Figs. 14a & 15a). The *c*-axis maximum 2 spreads out along a great circle roughly parallel to the flattening plane. The pole figures for the poles to the *r*- and *f*-planes also exhibit three maxima, again located at

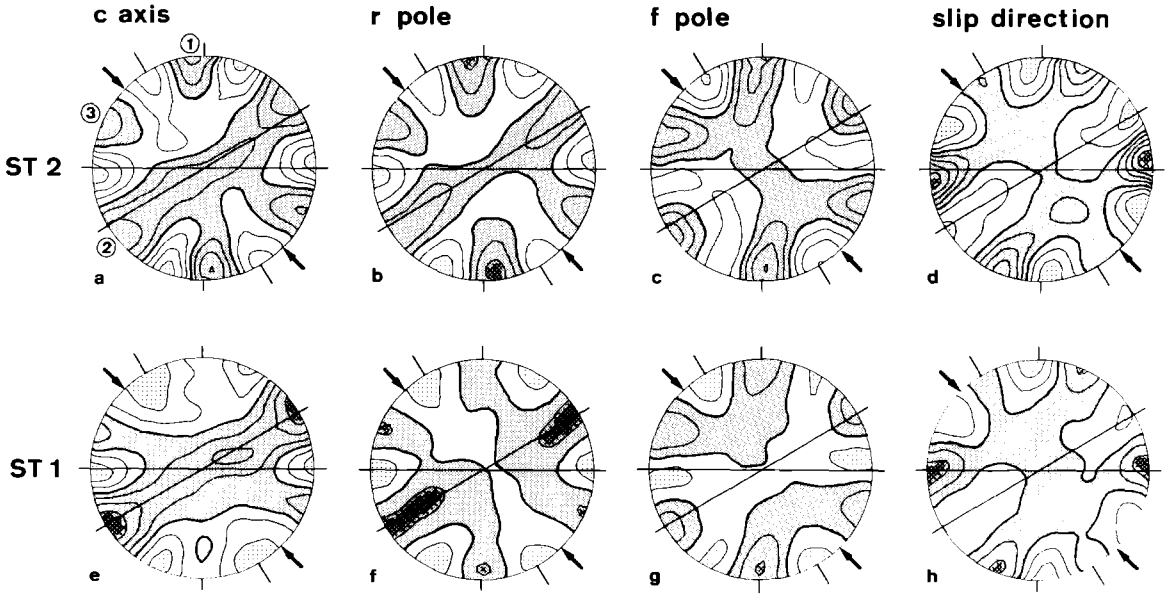

Fig. 14. Pole figures for Solnhofen limestone deformed in the intracrystalline slip regime at temperatures of 500°C (ST 2) and 700°C (ST 1). All pole figures are calculated from the ODF and contoured at intervals of 0.2 of a uniform distribution. The area with a density >1.0 is shaded. 'Slip direction' refers to the slip direction common to the *r*- and *f*-slip planes.

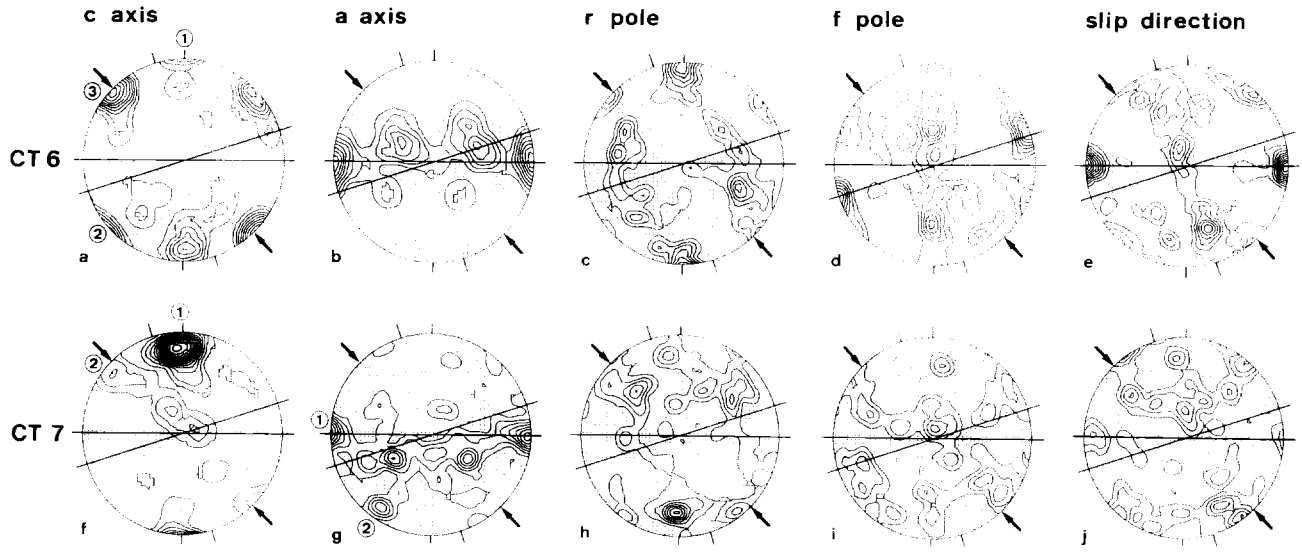

Fig. 15. Optically measured pole figures for Carrara marble deformed in the intracrystalline slip regime (CT 6, 700°C, top row) and in the grain-boundary migration regime (CT 7, 800°C, bottom row). The contour interval is 1.0 of a uniform distribution. 'Slip direction' refers to the slip direction common to the *r*- and *f*-slip systems. 15(b) includes only those *a*-directions which were measured for grains which have their *c*-axes aligned with the shear-zone boundary.

the margin of the pole figure and in positions which are almost identical with the positions of the *c*-axis maxima 1, 2 and 3. The pole figures of Fig. 14 are remarkably similar to those obtained by Kern & Wenk (1983).

In order to discuss the relationships between the pole figures for *r*, *f* and *c* it is useful to extract favoured crystal orientations from sections through the graphical representation of the ODF (Fig. 16). Again, the section at PHI = 90 (compare Fig. 13) is chosen because this section contains all the relevant information about crystals with their *c*-axis at the margin of the pole figure. Maximum 1 yields a favoured crystal orientation which is not very selective about the angle PSI 2 and which has a basal plane in an orientation with a critical resolved shear stress (i.e. near parallel to the shear-zone boundary). The high-intensity ridge corresponding to maximum 2 is curved. This means that different angles of PSI 2 are preferred at different positions in PSI 1. Two

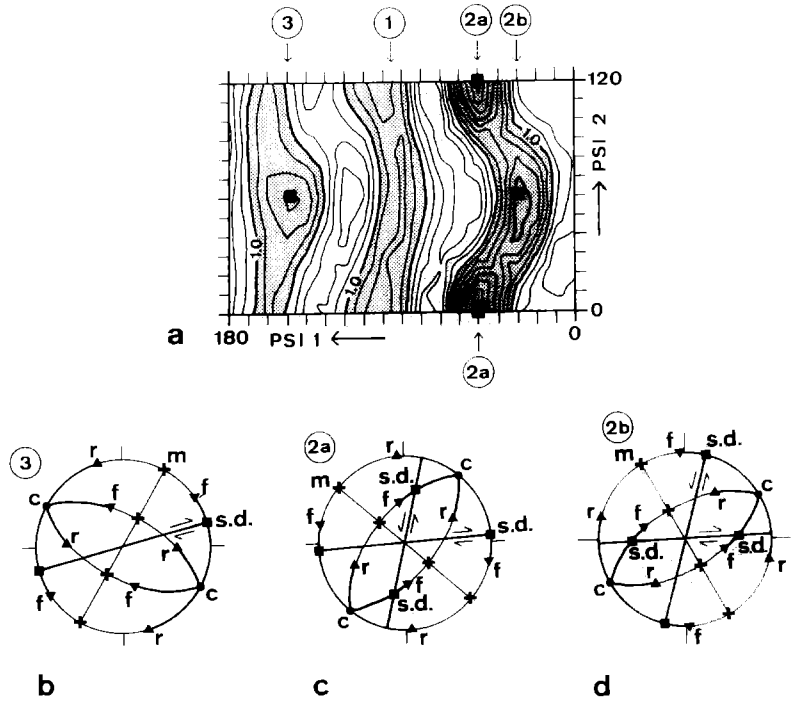

Fig. 16. Section through the ODF and favoured crystal orientations extracted from the ODF analysis of specimen ST 2, deformed in the intracrystalline slip regime (500°C). (a) Section at PHI = 90°. The crystal positions labelled 1, 2 and 3 correspond to the *c*-axis positions labelled with the same numbers in Fig. 14(a). Contour interval: 0.25 of a uniform distribution. Shaded area has a density of >1.0 of a uniform distribution. (b)–(d) Favoured crystal orientations corresponding to positions 3, 2a and 2b indicated in (a) (squares).

submaxima 2a and 2b were chosen from this ridge and plotted in Fig. 16(c) & (d). Position 2a corresponds to the most probable orientation in the entire ODF-space (2.9 times uniform) and locates one *r*-plane into near-parallelism with the shear plane and the slip direction at the periphery of the pole figure into near-parallelism with the shear direction of the simple shear experiment. Position 2b achieves the same for the *f*-plane. The *f*-plane contains two slip directions, and these are symmetrically disposed about the intersection point of *f*-plane and pole figure margin. Thus, in terms of the resolved shear stress both an *r*- and an *f*-plane are almost ideally oriented for easy slip in a positive sense. Thus, the *c*-axis position corresponding to maximum 2 is a mere consequence of the alignment of *r* and *f*. This *c*-axis maximum has not been observed in the twinning regime because it corresponds to an orientation with a high resolved shear stress for *e*-twinning, and consequently such *c*-axis positions were removed by twinning. *c*-axis maximum 3 yields a high resolved shear stress for negative slip on the *r*-plane and corresponds to a crystal orientation similar to the one observed in the twinning regime (Fig. 16b).

Thus *r*-, *f*- and the basal-plane are all nearly parallel to the shear-zone boundary, but systematically deflected away from strict parallelism in a counterclockwise sense. Since *r* and *f* are well established slip systems in calcite, it is tempting to interpret the texture development in terms of a progressive rotation of the active slip planes into parallelism with the shear-zone boundary. The observation that the basal plane of crystals with their *c*-axes parallel to maximum 1 also tend to be aligned with the shear zone boundary, suggests that basal slip was operative in addition to *r* and *f*. So far, strong evidence for basal slip in the direction of the *a*-axis has only been reported by Turner & Orozco (1976). Although the *a*-direction is parallel to the shortest Burgers vector in calcite (Paterson 1979) no other workers have reported basal slip.

Because the *r*-, *f*- and basal-planes are systematically deflected from ideal parallelism with the shear direction by a small angle, antithetic slip parallel to slip systems at a high angle to the shear-zone boundary has to operate in order to maintain bulk simple shear deformation. Indeed, the favoured crystal positions 2a and 2b (Fig. 16c & d) place *f* and *r*, respectively, into an orientation with high resolved shear stress for antithetic slip. This evidence for antithetic slip is also supported by the appearance of a second maximum in the pole figure for the slip direction of *r*- and *f*-slip systems at a high angle to the shear-zone boundary (Fig. 14d & h).

The inverse pole figures for the direction of σ_1 (Fig. 17a & d) show a remarkable similarity with some inverse pole figures obtained for the shortening direction in coaxial testing. In the absence of twinning a maximum in the region around the *e*-plane normal combined with a ridge running from the *a*- to the *h*-plane normals has been observed by Casey *et al.* (1978) for Solnhofen limestone deformed in flow regimes 1 and 2, and by Wenk *et al.* (1973) under similar experimental conditions.

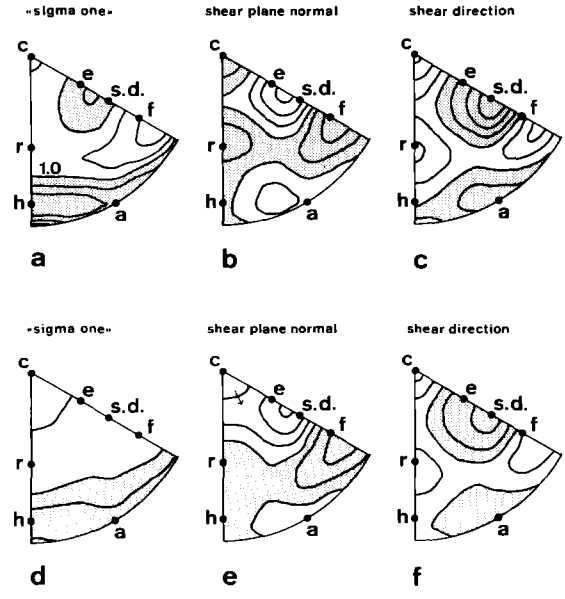

Fig. 17. Inverse pole figures for selected directions for specimens ST 2 (a), (b), (c) and ST 1 (d), (e), (f) deformed in the intracrystalline slip regime. Contour interval: 0.2 of a uniform distribution. Area with a density >1.0 shaded. The crystal direction labelled s.d. corresponds to the slip direction of both the *r*- and *f*-slip planes.

The parallelism of slip planes and slip directions with the shear-zone boundary and shear direction of the simple shear experiment is most readily visualized with the help of inverse pole figures for the normal to the shear-zone boundary and the shear direction (Fig. 17b, c, e & f). The inverse pole figure for the normal to the shear-zone boundary shows three maxima parallel to the poles to *r*-, *f*- and the basal-plane. The inverse pole figure for the shear direction shows two maxima parallel to the common slip direction of *r* and *f* and parallel to the *a*-direction (the slip direction of the basal plane).

The results of the optical measurements on Carrara marble specimen CT 6 (Fig. 15 a–e) additionally support the evidence from the X-ray analysis on Solnhofen limestone specimens ST 2 and ST 1. The *a*-axes of those grains which have their *c*-axis aligned with maximum 1 show strict parallelism with the shear direction (Fig. 15b). The poles to the *r*-planes exhibit a maximum exactly parallel to the normal to the shear-zone boundary and the slip direction for *r* and *f* is parallel to the shear direction of the simple shear experiment (Fig. 15c & e). The second maximum in the pole figure for the slip directions of *r* and *f* at a high angle to the shear-zone boundary, observed in ST 2 and ST 1 (compare Fig. 14d & h), has almost completely disappeared (Fig. 15e). This specimen CT 6 suffered a shear strain ($\gamma = 2.85$) very much larger than the shear strains applied to specimens ST 2 and ST 1 ($\gamma = 1.22$ and 1.07, respectively). Thus, the active slip systems are inferred to progressively rotate into strict parallelism with the shear-zone boundary after large amounts of strain. Consequently, activity on the antithetically operating slip system is no longer needed.

In conclusion, there is strong evidence for: (1) the activity of *r*-, *f*- and basal-slip in the 'intracrystalline slip

regime'; and (2) a texture development towards an end-orientation for easy slip after large shear strains (parallelism of active slip systems and shear-zone boundary) which remains stable since the vorticity of slip parallel to the ideally aligned slip system is now identical with the vorticity of the imposed deformation.

THE GRAIN-BOUNDARY SLIDING REGIME

Microstructural characteristics

This microfabric regime is associated with flow regime 3 for Solnhofen limestone, where grain-boundary sliding is the main deformation mechanism (Schmid *et al.* 1977). It was not observed in Carrara marble. Solnhofen limestone deformed in this regime (700–900°C, ST 5, ST 7 and ST 4) exhibits some grain growth. The dominant microstructural features, however, are: (1) the equilibration of originally serrate into straight grain boundaries; and (2) the absence of a strong shape anisotropy of individual grains reflecting the imposed strain (Fig. 8h). Clearly, the equilibration of the grain boundaries is brought about by grain-boundary migration. But, in contrast to the Carrara marbles deformed at the higher temperatures (described in a later section), grain boundary migration merely leads to an equilibration of grain boundaries and not to significant grain growth (compare Fig. 8e & h).

The microstructural changes from the intracrystalline slip regime into the grain-boundary sliding regime are gradual. No direct microstructural evidence for grain-boundary sliding was found on the basis of the present experiments. The rheological results, however, demonstrated that specimens ST 5, ST 7 and ST 4 were deformed near or within flow regime 3 (grain-boundary sliding). The microstructural characteristics of these specimens deformed in simple shear are virtually identical with those described by Schmid *et al.* (1977) for the same flow regime. Both rheological considerations and microstructural investigations using the split cylinder technique led Schmid *et al.* (1977) to conclude that grain boundary sliding is the dominant deformation mechanism in flow regime 3. It is mainly on the basis of the strong rheological and microstructural similarities between coaxial and simple shear experiments that grain boundary sliding is inferred to be the dominant deformation mechanism in the Solnhofen limestone specimens deformed at the highest temperatures. The following texture analysis will give additional support for such an interpretation.

Texture analysis

In the *c*-axis pole figures for specimens deformed in this regime (700–900°C, ST 5, ST 7 and ST 4) the maxima 1 and 3, observed in the intracrystalline slip regime, disappear (Fig. 18). At the same time maximum 2 is maintained but starts to spread out more strongly along a great circle oriented approximately parallel to the flattening plane. The pole figures for *r*, *f* and the slip direction of *r* and *f* become gradually more random

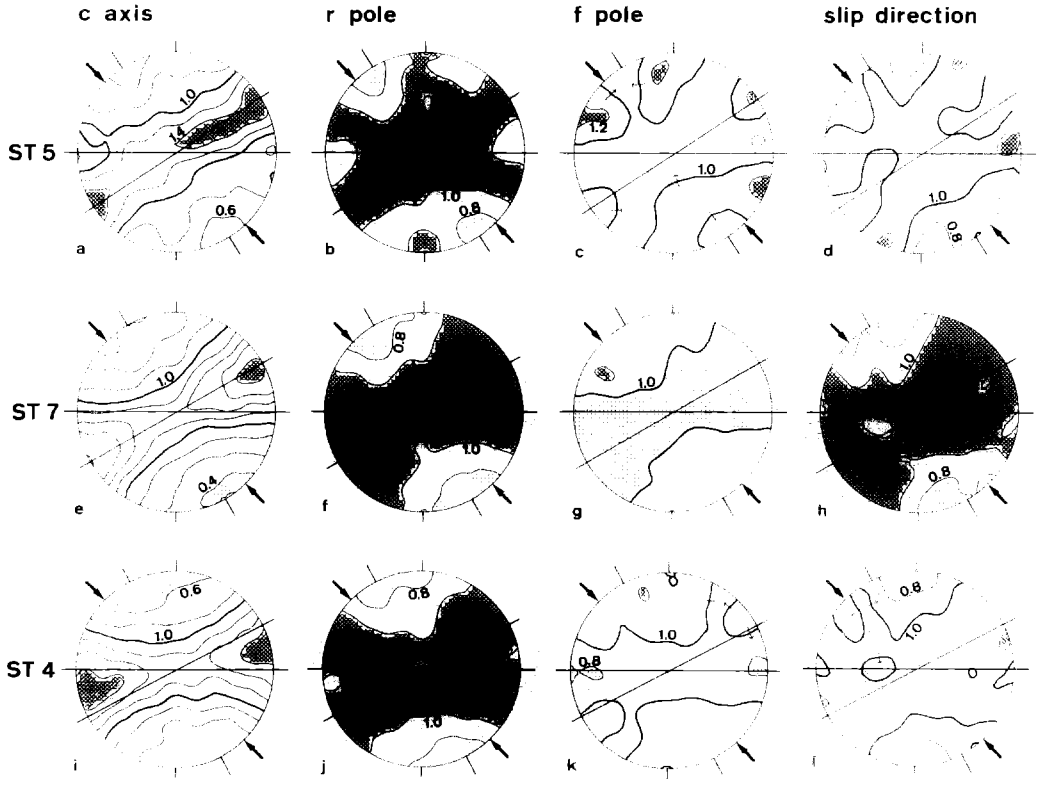

Fig. 18. Pole figures for Solnhofen limestone deformed in the grain-boundary sliding regime. All pole figures are calculated from the ODF and contoured at intervals of 0.2 of a uniform distribution. 'Slip direction' refers to the slip direction common to the *r*- and *f*-slip planes.

towards the higher temperatures (i.e. from top to bottom in Fig. 18). The pole figures for ST 5 (Fig. 18a–d), i.e. for the specimen deformed near the transition from flow regime 2 into flow regime 3 (compare Fig. 6) still show the essential characteristics of the specimens deformed in the intracrystalline slip regime (i.e. ST 2 and ST 1, Fig. 14). Thus, the change in texture is gradual and some features of the texture found in the intracrystalline slip regime are maintained in the grain-boundary sliding regime. This strongly suggests that a minor fraction of the total strain is still taken up by intracrystalline slip.

The inverse pole figures for the direction of σ_1 (Fig. 19) are again virtually identical to some of the inverse pole figures found in coaxially deformed Solnhofen limestone. Casey *et al.* (1978) described an identical pattern with a maximum at a high angle to the *c*-axis for Solnhofen limestone deformed in regime 3. Lister (1978) successfully simulated such a pattern by activating *f*-slip only, using the Taylor–Bishop–Hill analysis.

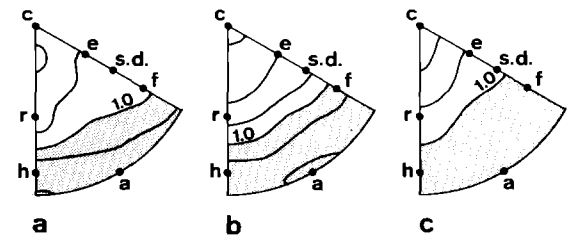

Fig. 19. Inverse pole figures for the specimen direction coinciding with σ_1 for Solnhofen limestone specimens deformed in the grain-boundary sliding regime. Contour interval: 0.2 of a uniform distribution. Area with a density >1.0 shaded. (a) Specimen ST 5 (700°C), (b) specimen ST 7 (800°C) and (c) specimen ST 4 (900°C).

In order to extract selected crystal orientations and to demonstrate the gradual change in texture more clearly it is again useful to discuss some selected sections through the graphical representation of the ODF (Fig. 20). According to the convention of Eulerian angles used for the texture analysis (Casey 1981) the sections at

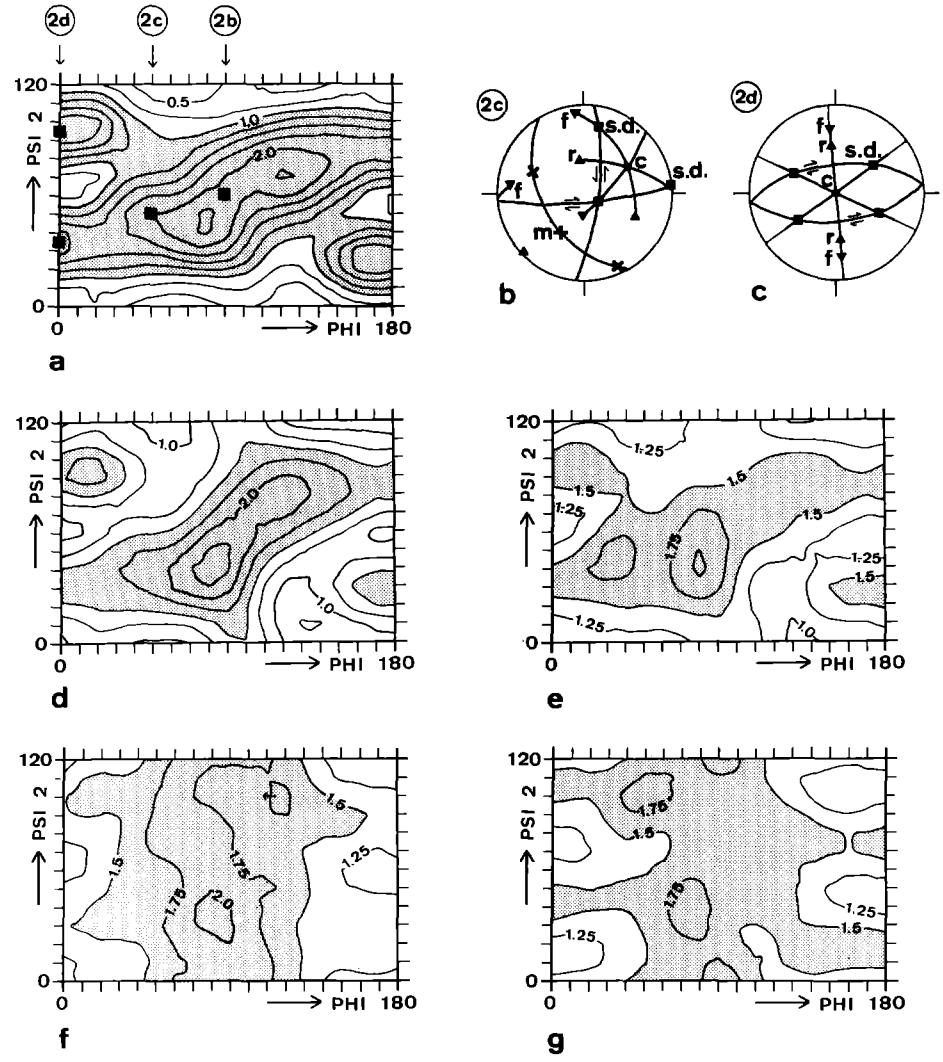

Fig. 20. Sections through the graphical representation of the ODF illustrating the transitional character of the texture across the boundary from the intracrystalline slip regime (a), (d) into the grain-boundary sliding regime (e)–(g) in Solnhofen limestone. The chosen sections correspond to an angle PSI 1 = 30° (a), (d), (e), (f) and PSI 1 = 20° (g). Contour interval: 0.25 of a uniform distribution; area with a density >1.0 of a uniform distribution (a), or 1.5 of a uniform distribution (d), (e), (f), (g) shaded. (a) Specimen ST 2 (500°C, intracrystalline slip regime). The solid squares indicate the Eulerian angles used for plotting the favoured crystal orientations displayed in Fig. 16(d) (position 2b), and their figure (b) (position 2c), and (c) (position 2d). (b), (c) Favoured crystal orientations corresponding to positions 2c and 2d indicated in (a). (d) Specimen ST 1, deformed in the intracrystalline slip regime. (e), (f), (g) Specimens ST 5 (e), ST 7 (f), and ST 4 (g), deformed in the grain-boundary sliding regime at temperatures of 700, 800 and 900°C, respectively.

an angle of PSI 1 = 20° (ST 4) and PSI 1 = 30° (all other specimens in Fig. 20) contain the complete information on the preferred orientation of crystals with their *c*-axes on a great circle inclined by 20 and 30°, respectively, with respect to the shear-zone boundary. This great circle corresponds to the high density area in the *c*-axis pole figures found in the grain-boundary sliding regime.

Because some of the features of the section at PSI 1 = 30°, found in specimen ST 2 (intracrystalline slip regime), are maintained in all the specimens deformed in the grain-boundary sliding regime, it is useful to extract some additional favoured crystal orientations from this section on ST 2. The high-density ridge running obliquely through the diagram (Fig. 20a) clearly demonstrates a high degree of selectivity in terms of favoured crystal orientations for crystal directions other than the *c*-axis. The *c*-axis position at PHI = 90° strongly favours an angle PSI 2 = 60°, corresponding to the favoured crystal orientation previously extracted from a perpendicular section through the same ODF at PHI = 90° (compare Fig. 16, position 2b). This position was found to result in a high resolved shear stress for the *f*-plane. The *c*-axis position 2c (Fig. 20b) has two *f*-planes in an orientation of high resolved shear stress, one of them favourably oriented for synthetic slip. The *c*-axis position 2d favours two angles in PSI 2, 60° apart in terms of PSI 2. These maxima again correspond to orientations with a high resolved shear stress on *f*-planes (Fig. 20c). In summary, all the *c*-axis positions along the great circle subparallel to the flattening plane correspond to crystal orientations with high resolved shear stress on *f*-planes.

Figure 20 demonstrates that the selectivity in terms of a preferred angle PSI 2 is gradually lost as one moves into the grain-boundary sliding regime. In other words, only the *c*-axes remain in a preferred orientation whereas crystal directions other than *c* gradually lose their preferred orientation. This observation is not easy to interpret. An interpretation is difficult because there must be a complicated interplay between two mechanism of lattice rotation: (1) external rotation of grains caused by *f*-slip, whereby the individual grains are completely free to rotate relative to neighbouring grains due to the simultaneous operation of grain-boundary sliding; and (2) rotations of grains due to the randomizing effect of grain-boundary sliding and not controlled by the activity of particular slip systems. Thus, grain-boundary sliding may speed up slip-induced lattice rotations because the grains are unconstrained by their neighbours, and simultaneously randomize the texture due to crystallographically uncontrolled rotations.

In spite of the difficulties in the exact interpretation of the observed textures, this analysis provides strong evidence for the simultaneous activity of *f*-slip during grain-boundary sliding. Together with minor amounts of grain-boundary migration, *f*-slip helps to provide the necessary accommodations of grain boundaries during grain-boundary sliding. Thus, there is no need for solid state diffusion as an accommodating mechanism (Ashby & Verrall 1973).

THE GRAIN-BOUNDARY MIGRATION REGIME

Microstructural characteristics

This microstructural regime was only observed in Carrara marble. At the highest temperatures (800–900°C) substantial amounts of grain growth occur in specimens CT 2, CT 7 and CT 4 due to dynamic recrystallization by grain-boundary migration (Guillope & Poirier 1979). In contrast to the findings on Solnhofen limestone, grain-boundary migration tends to produce highly irregular grain boundaries (Fig. 8e & f). Thus, the equilibration of grain boundaries cannot be the driving force for grain-boundary migration in Carrara marble.

An alternative driving mechanism for grain-boundary migration is the difference in the amount of elastic energy stored within two neighbouring grains due to a difference in dislocation density. Thereby grains (or parts of grains) with low distortional strain energy grow at the expense of grains with a high distortional strain energy.

A second mechanism of dynamic recrystallization dominating in the intracrystalline slip regime, subgrain rotation (Hobbs 1969), now acts simultaneously with migration recrystallization. A similar trend was observed on Carrara marble coaxially deformed in flow regimes 2 and 3 (Schmid *et al.* 1980).

In specimen CT 7, deformed to the very high shear strain $\gamma = 2.74$, migration recrystallization proceeded fastest near the interface with the driving blocks (Fig. 8e). The reasons for this remained unclear. Figure 8(e) shows that this same region appears in the form of two dark rims near the interface. In this rim region all the *c*-axes are oriented perpendicular to the shear-zone boundary, hence all grains are in extinction. This observation is important in suggesting that extensive grain-boundary migration recrystallization goes hand in hand with a high degree of preferred orientation.

Texture analysis

The texture of the highly deformed and completely recrystallized specimen CT 7 (800°C) was measured along traverses across the shear zone in order to incorporate equal numbers of grains within the center and the rim of the shear zone. The *c*-axis pole figure exhibits a very strong *c*-axis maximum perpendicular to the shear-zone boundary and a weaker girdle across the pole figure (Fig. 15f). This strong maximum perpendicular to the shear-zone boundary corresponds to maximum 1 found in the *c*-axis pole figures of specimens deformed in the intracrystalline slip regime (Fig. 15a). With respect to the plane of finite flattening, the *c*-axis fabric of this specimen is very reminiscent of quartz *c*-axis crossed girdles (Schmid & Casey 1986). The dominating girdle (in the case of CT 7 reduced to a maximum at the periphery of the pole figure) is deflected from the normal to the flattening plane in a clockwise sense, i.e. with the sense of shear. The weaker girdle is deflected counterclockwise.

The pole figure for the *a*-direction shows an almost perfect alignment of one of the *a*-axes with the shear direction (Fig. 15g). Thus a perfect alignment of the basal-plane and the *a*-direction with the shear-zone boundary and shear direction is observed, in agreement with the findings for the *c*-axes corresponding to maximum 1 in specimen CT 6 (deformed in the intracrystalline slip regime). The pole figures for *r*, *f* and the slip directions of *r* and *f* are less distinct in comparison with specimen CT 6 (Fig. 15 h–j). Therefore, basal slip in the *a*-direction is interpreted to be the dominating deformation mechanism in the grain-boundary migration regime. This also explains the similarities with quartz *c*-axis pole figures since basal slip in the *a*-direction is an important slip system in quartz.

The crystals with their *c*-axes parallel to the weaker cross girdle (position 2 in Fig. 15f) preferentially place one *a*-direction at the margin of the pole figure (position 2 in Fig. 15g). This suggests that this weaker cross girdle formed during the initial stages of deformation, when the dominating maximum 1 was not yet ideally aligned with the shear-zone boundary and antithetic slip had to operate in order to maintain simple shear boundary conditions.

The earlier mentioned microstructural observation that the higher rate of migration recrystallization near the sandstone marble interface goes together with a higher degree of preferred orientation, gives support to a model proposed by Schmid & Casey (1986) based on the interpretation of quartz textures. Migration recrystallization selectively consumes grains with a high distortional lattice energy, i.e. grains unfavourably oriented for easy slip. Thus, migration recrystallization very efficiently establishes an end orientation for easy slip. This in turn leads to work softening, as observed for the specimens deformed in the grain-boundary migration regime (compare Fig. 5).

NUMERICAL MICROSTRUCTURAL ANALYSIS

Techniques and data representation

Thin sections of the calcite shear zones were prepared normal to the shear-zone boundary and parallel to the direction of shear displacement. The *x*-direction is parallel to the shear-zone boundary, *y* is normal to it, the angle of orientation, α, is 0° in the direction of shear. Photographic enlargements were made at the scale of about 1000 : 1 in the case of Solnhofen limestone, and of about 70 : 1 in the case of Carrara marble. The photographs were placed on an Apple digitizing tablet with a linear resolution of 20 l/mm. The grain boundaries of the grains were traced, reading co-ordinates at a distance of 0.5 or 1 mm, respectively, i.e. at a real distance of 0.5 or 15 μm, respectively. Thus for every grain, an average of about 50 points were recorded. Due to the small grain size of Solnhofen limestone, only the largest grains on a given area could be digitized, whereas for Carrara marble all grains of a geometrically coherent area could be evaluated.

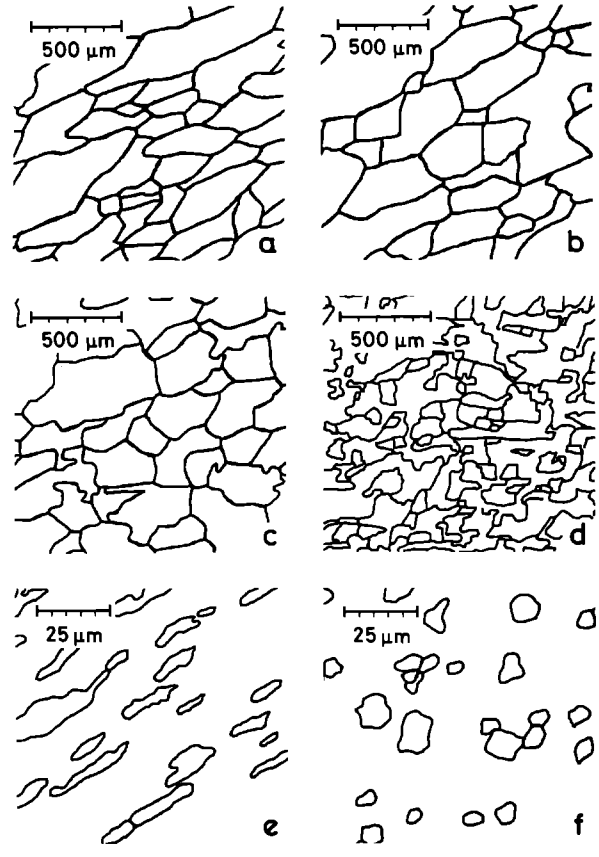

Fig. 21. Digitized grain-boundary outlines of deformed Carrara marble (a)–(d) and Solnhofen limestone (e), (f). (a) CT 1, 600°C, twinning regime; (b) CT 3, 700°C, intracrystalline slip regime; (c) CT 2, 800°C, grain-boundary migration regime; (d) CT 4, 900°C, grain-boundary migration regime; (e) ST 2, 700°C, intracrystalline slip regime; (f) ST 4, 900°C, grain-boundary sliding regime.

A quantitative microstructural analysis was carried out using the projection method introduced by Panozzo (1984); for summary of method and details of procedure, see Appendix 2. In the process of digitization, the grain-boundary outlines were approximated by strings of small straight line segments. Digitized grain-boundary outlines are shown in Fig. 21. The shape of these strings of line segments, which correspond to the linear traces of the grain-boundary surface, and the shapes of the included polygons, which correspond to the sectional areas of the individual grains, were evaluated quantitatively (see Appendix 2). Thus, two different types of fabric were defined, which allow two types of strain interpretation: (1) assuming that the grain-boundary *surfaces* acted as passive markers; and (2) assuming that the individual grain *volumes*, i.e. their shapes, acted as passive markers during the deformation. In many cases, grain-boundary surface strain and grain-volume strain coincide, indicating that the individual grain volumes and their corresponding surfaces deformed as a physically coherent entity. In these cases, one type of analysis can be substituted for the other. However, as soon as deformation mechanisms start to occur which specifically modify the shape of the grain-boundary surface (involving, e.g. grain-boundary migration), surface strain and grain-volume strain are likely to differ.

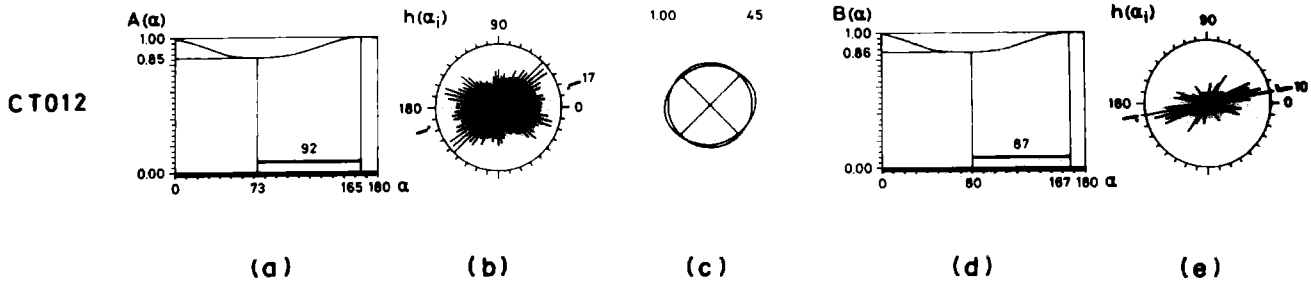

Fig. 22. Results of surface analysis and grain-volume analysis. Columns from left to right: (a) surface projection diagram $A(\alpha)$; (b) surface rose diagram; (c) characteristic shape and superposed strain ellipse (with strain axes); (d) projection diagram of grain volume, $B(\alpha)$; (e) rose diagram of long axes of grains. In the projection diagrams, the numerical values for $A(\alpha)_{min}$, $B(\alpha)_{min}$, α_{min} and α_{max} are indicated as shown in Fig. A1. The rose diagrams show the values for the preferred orientation, $\alpha_p = 90° - \alpha_{min}$, of surface and grain-volume fabrics. The dashed line indicates the theoretical orientation of the strain ellipse. CT 012 is the undeformed Carrara marble.

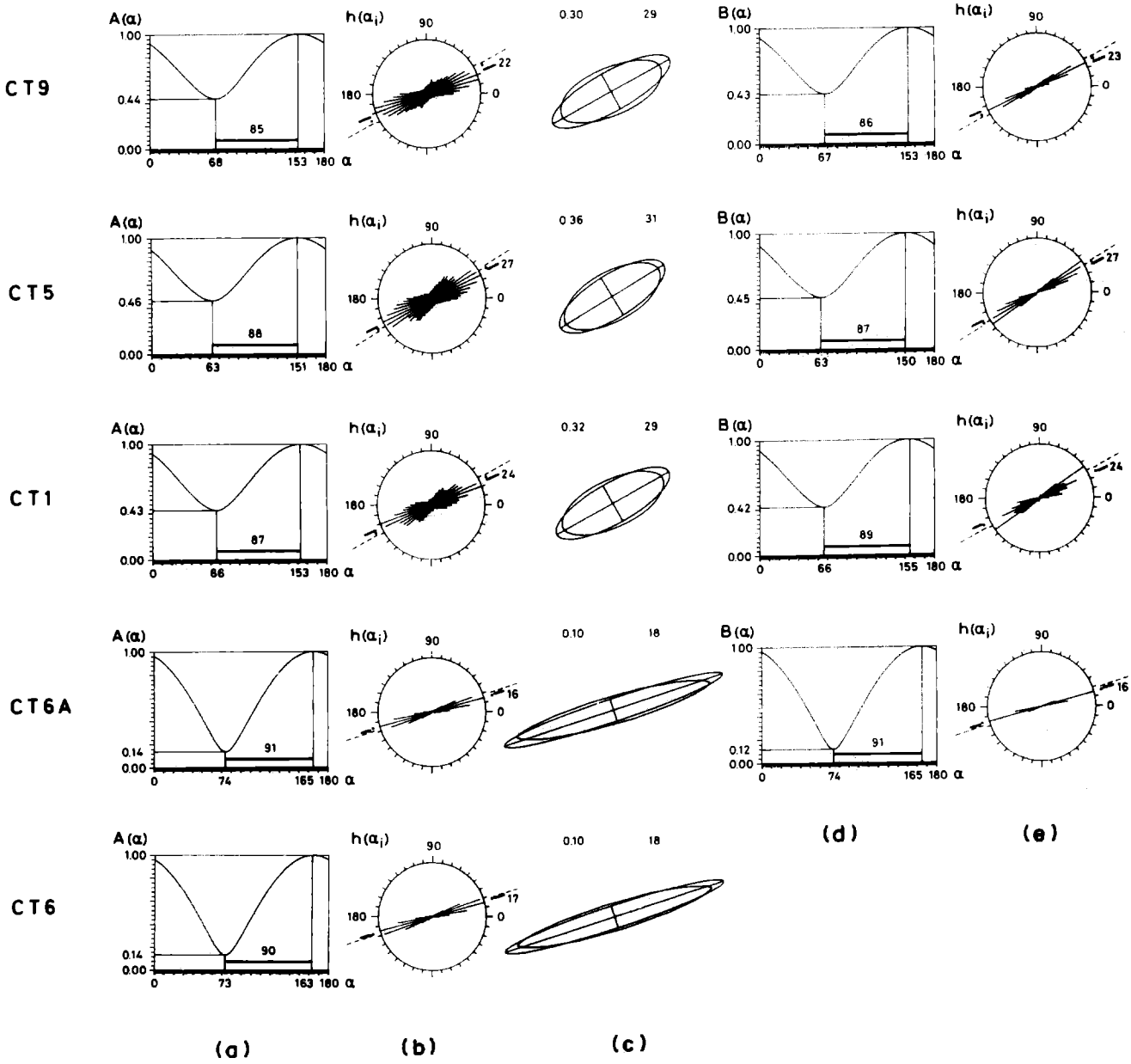

Fig. 23. Results of surface analysis and grain-volume analysis (analogous to Fig. 22). Samples are Carrara marble: CT 9 (350°C), CT 5 (500°C), and CT 1 (600°C) are deformed in the twinning regime; CT 6 (700°C) and CT 6A (700°C) are deformed in the intracrystalline slip regime. CT 6A is the same as CT 6, except that for CT 6A only the complete grain boundaries were used for fabric analysis.

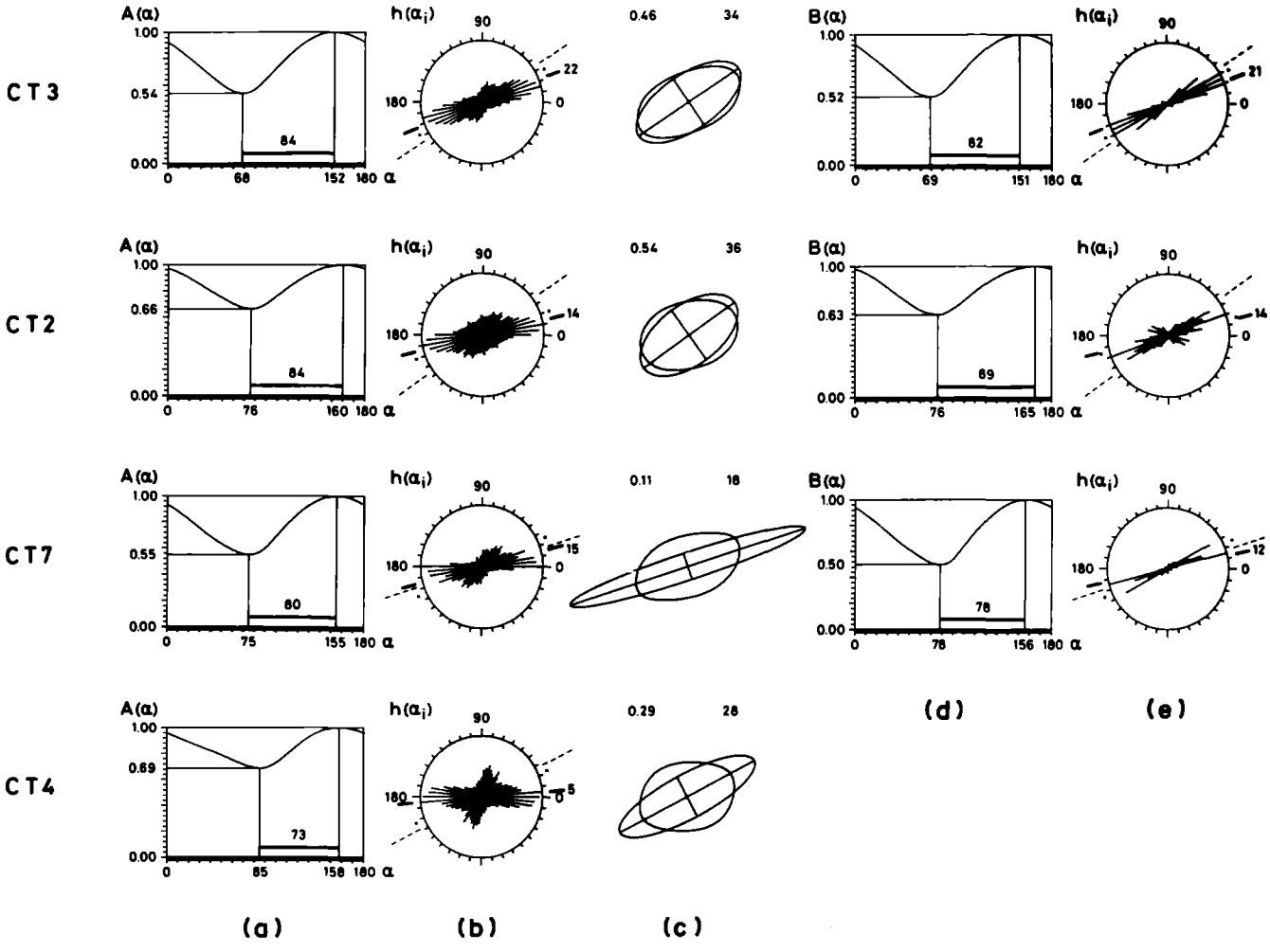

Fig. 24. Results of surface analysis and grain-volume analysis (analogous to Fig. 22). Samples are Carrara marble. CT 3 (700°C) is deformed in the intracrystalline slip regime; CT 2 (800°C), CT 7 (800°C) and CT 4 (900°C) are deformed in the grain-boundary migration regime.

Results of surface analysis are given as rose diagrams representing the two-dimensional orientation distribution function of grain-boundary surface, and as projection diagrams representing the total length of projection of the grain-boundary surface per angle of rotation (functions $h(\alpha_i)$ and $A(\alpha)$ in columns (b) and (a) of Figs. 22–25). To better visualize the 'average' grain shape that is implied by the result of a given surface analysis, the characteristic shape is shown in column (c) of Figs. 22–25 (for definition of characteristic shape, see Appendix 2). Results of the analysis of grain volumes are given as rose diagrams representing the total length of long axes of grains per angle of orientation and as projection diagrams representing the total length of projection of the grains per angle of rotation (functions $h(\alpha_i)$ and $B(\alpha)$ in columns (e) and (d) in Figs. 22–25). Table 3 lists the numerical results of the fabric analysis.

Interpretation of the fabrics in terms of strain entailed three separate steps. The first was to determine from the results of the fabric analysis whether a given fabric could at all be interpreted in terms of strain. The following criteria were used: (a) symmetry and unimodality of the orientation distribution function of surface; (b) symmetry and unimodality of the projection functions $A(\alpha)$ and $B(\alpha)$, in particular, whether or not the minima and maxima of these curves are 90° apart. To account for sampling errors, a $\Delta\alpha$ between 85 and 95° was accepted. The axial ratio of the fabric ellipse was then given as b/a, where b corresponds to the short axis, and a to the long axis. The second step was to compare the strains inferred from the surface analysis with those obtained from the grain-volume analysis. The third step was to compare the strains obtained from either of these two fabrics with the applied shear strain, γ, which was calculated from the applied shear displacement.

General observations: projection of grain-boundary surface vs projection of individual grains

There is a remarkable coincidence between the projection diagrams obtained from surface analysis and those obtained from grain-volume analysis (see columns (a) and (d) of Figs. 22–25). The surface projection diagrams, $A(\alpha)$, and the grain projection diagrams, $B(\alpha)$, yield practically the same values for b/a, the ratio of shortest over longest projection, and the same orientations, α_p, of the fabric ellipse (see columns (5) and (6) of Table 3). The advantage of this is that the surface

Table 3. Results of fabric analysis

Sample	(γ)	(1) Theoretical b/a	(1) Theoretical α_p(°)	(2) S	(3) M	(4) $\Delta\alpha$	(5) Surface b/a	(5) Surface α_p(°)	(6) Particle b/a	(6) Particle α_p(°)
ST 2	1.22	0.32	29	+	+	+	0.36	31	0.32	30
ST 1	1.07	0.36	31	+	+	+	0.57	33	0.54	32
ST 5	0.92	0.41	33	+	0	+	0.69	28	0.68	26
ST 4	1.36	0.28	28	—	—	—	0.85	(28) *	0.84	(27) *
CT 012	0.00	1.00	45	0	0	+	0.85	(17) *	0.86	(10) *
CT 9	1.27	0.30	29	0	+	+	0.44	22	0.43	23
CT 5	1.08	0.36	31	+	+	+	0.46	27	0.45	27
CT 1	1.22	0.32	29	+	+	+	0.43	24	0.42	24
CT 6A †	2.85	0.10	18	+	+	+	0.14	16	0.12	16
CT 6	2.85	0.10	18	+	+	+	0.14	17	— ‡	— ‡
CT 3	0.79	0.46	34	—	—	—	0.54	22	0.52	21
CT 2	0.63	0.54	36	—	—	—	0.66	14	0.63	14
CT 7	2.74	0.11	18	—	—	—	0.55	15	0.50	12
CT 4	1.31	0.29	28	—	—	—	0.69	05	— ‡	— ‡

(γ) Applied shear strain, calculated from the measured displacements.
(1) Theoretical values for axial ratio, b/a (= short axis/long axis), and preferred orientation, α_p, calculated for given γ.
(2) Symmetry of orientation distribution function, $h(\alpha_i)$. + = symmetric, 0 = undecided, — = asymmetric.
(3) Modality of orientation distribution function, $h(\alpha_i)$. + = unimodal, 0 = undecided, — = bimodal.
(4) Angular difference, $\Delta\alpha$, of minimum and maximum value of projection function, $A(\alpha)$. + = ($85° < \Delta\alpha < 95°$). — = ($85° > \Delta\alpha$) or ($\Delta\alpha > 95°$).
(5) Axial ratio, b/a (= short axis/long axis), and preferred orientation, α_p, calculated from α_{min} of surface fabric.
(6) Axial ratio, b/a (= short axis/long axis), and preferred orientation, α_p, calculated from α_{min} of particle fabric.
* Angle is not well defined because of large ratio b/a.
† Same as CT 6, using complete outlines only.
‡ Particle evaluation impossible.

fabric can be substituted for the grain-volume fabric and that, in this case, an area of analysis can be defined without having to worry about whether or not certain grain boundaries will be truncated at the border of the measuring area. The latter is important in cases where mineral grains are so highly elongated that their length is greater than the diameter of the measuring area (e.g. CT 6) or where the connected individual grain volumes cannot be identified because of intensive grain-boundary migration (e.g. CT 4).

The coincidence between the projection curves $A(\alpha)$ and $B(\alpha)$ generally indicates that the grains are not very serrated. Theoretically, the grain boundaries could still be serrated, but in this case, the preferred orientation of the grain boundaries could not be different from that of the individual grain volumes.

General observations: rose diagrams of grain-boundary surface vs rose diagrams of long axes of grains

The differences between the rose diagrams obtained from surface analysis and those obtained from grain-volume analysis (columns (b) and (e), Figs. 22–25) are partly due to statistics. Sample size for the long axes of grains is of the order of 50–80 per analyzed fabric. Sample size for surfaces (i.e. number of digitized line segments) is usually between 3000 and 5000 per analyzed fabric. While displaying a smoother orientation distribution function the surface rose diagrams also indicate a wider directional scatter. This is generally to be expected: long axes of mineral grains will display less scatter than the corresponding surface elements because even in the case where grains have strictly parallel long axes, the surface will have fractions that are not oriented parallel to that direction.

At higher temperatures the rose diagrams of surface analysis display bimodal asymmetric orientation distributions which are not detected in the rose diagrams of the grain axes. This indicates independent deformational behaviour of grain volumes and grain-boundary surfaces (Figs. 24 and 25), and will be discussed later.

Characteristic shape and theoretical strain ellipse

The characteristic shapes of the fabrics are shown superposed with the theoretical strain ellipse (column (c), Fig. 22–25). Both are scaled such that their areas are of unit size. The theoretical strain ellipse is derived from the applied displacements. The numbers of the theoretical values of the axial ratio and the orientation of the long axis are shown to the left and right, respectively. If the preferred orientation of the grain boundaries were entirely due to deformation, and if the initial state were one of random orientation of surface, the characteristic shape and the strain ellipse should coincide.

Two types of deviations are observed. In some cases

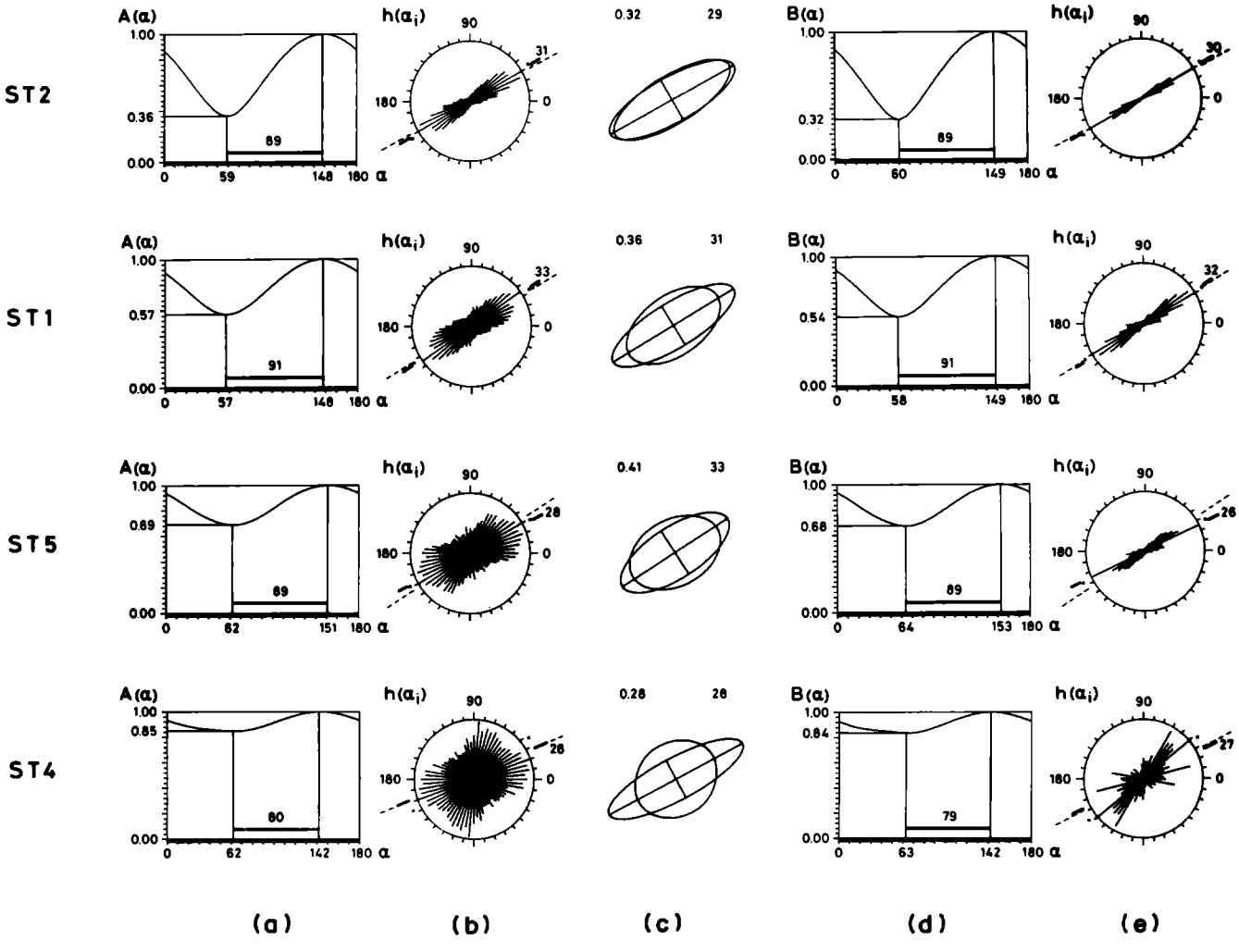

Fig. 25. Results of surface analysis and grain-volume analysis (analogous to Fig. 22). Samples are Solnhofen limestone. ST 2 (500°C) and ST 1 (700°C) are deformed in the intracrystalline slip regime; ST 5 (700°C) and ST 4 (800°C) are deformed in the grain-boundary sliding regime.

(typically for the low temperature samples), the characteristic shapes are elliptical, but the axial ratios and orientations differ from the theoretical values; in other words, the values of strain inferred from these surface fabrics would be incorrect. In other cases (typically for high temperature samples), the characteristic shape is asymmetric, which indicates that the surface fabric does not reflect strain.

Results for Carrara marble from the twinning to the intracrystalline slip regime

The starting material, i.e. the undeformed sample (CT 012), displays a weakly developed anisotropy in both the surface fabric and the grain-volume fabric (see Fig. 22). The material has been analyzed at various sites; the values for the axial ratio, *b/a*, of the fabric ellipse is

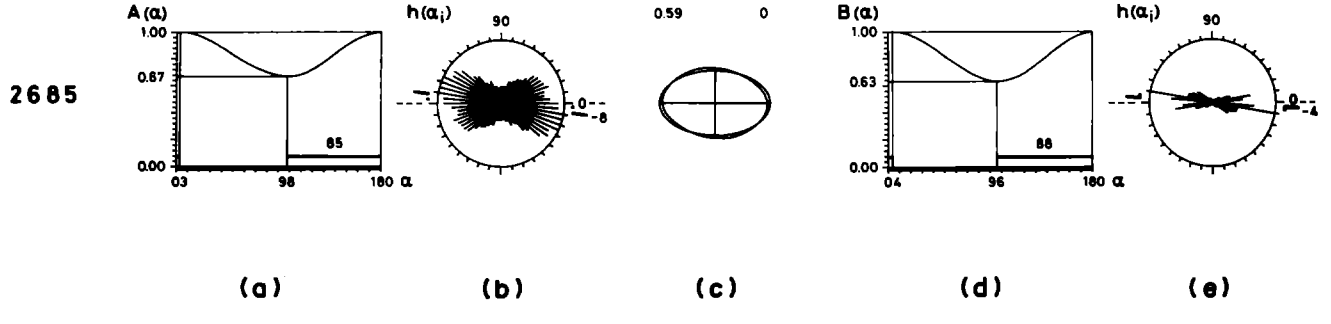

Fig. 26. Results of surface analysis and grain-volume analysis (analogous to Fig. 22). Sample is an inclined dextral shear zone within coaxially deformed Carrara marble (Schmid *et al.* 1977.

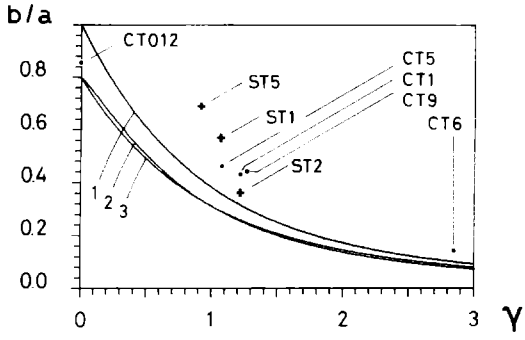

Fig. 27. Diagram of the axial ratio of the strain ellipse (or characteristic shape) vs shear strain. Curves represent theoretical values: (1) for shear deformation of circle (i.e. fabric with initial random orientation of surface); (2) and (3) for shear deformation of ellipse (i.e. fabric with initial preferred orientation of surface). Axial ratio, b/a, of fabric ellipses is 0.80, initial orientation: $\alpha_i = 43°$ (2) and $\alpha_i = 73°$ (3).

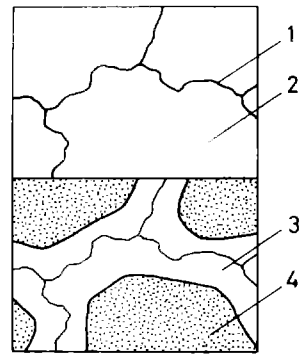

Fig. 28. Schematic representation of visually defined and mechanically defined grains and grain boundaries. (1) Visually defined grain boundary, (2) visually defined grain, (3) mechanical grain boundary (zone), (4) mechanically coherent grain.

typically between 0.80 and 0.90; the direction of the preferred orientation ranges between 43 and 73° with respect to the shear-zone boundary. This indicates that the initial fabric is not perfectly isotropic or, in terms of strain, is not completely undeformed. However, the effect of this initial fabric can be neglected (see Appendix 3 for discussion).

For CT 9 (350°C), CT 5 (500°C), CT 1 (600°C) and CT 6 (700°C), the distribution of grain-boundary surfaces is symmetric, and the characteristic shape, apart from digitizing errors, is an ellipse (see Fig. 23). However, if an interpretation in terms of strain is carried out one finds that the axial ratio, b/a, is consistently too high for all samples: compare the shape and orientation of the characteristic shapes and the superposed theoretical strain ellipses in column (c) of Fig. 23. Similarly, the angle of orientation, α_p, is consistently too low: compare the preferred orientation indicated in the rose diagrams with the theoretical values shown as dashed lines, column (b) and (e) of Fig. 23. These deviations from the theoretical values cannot be explained in terms of the pre-existing anisotropy of the initial fabric (see Appendix 3). As a matter of fact, if the initial fabric were taken into account, the deviation from the theoretical values would have to be considered even more significant (see Fig. 27).

There is also a remarkable coincidence between the results obtained from the surface analysis and those of grain-volume analysis. For a given sample, both the axial ratio, b/a, and the angle of orientation, α_p, determined from the surface fabric and from the grain volumes are practically the same. Thus the deviation of the fabric ellipse from the theoretical values of the strain ellipse is significant.

CT 9 (350°C), CT 5 (500°C) and CT 1 (600°C) have been deformed in the twinning regime (*e*-twinning and *r*-slip). On a two-dimensional section parallel to the shear direction, twinning leads to non-plane strain on the scale of individual grains (see Fig. 11), in other words, grains with too high an axial ratio in the x–y plane of the thin section are to be expected. On the other hand it was demonstrated earlier that the bulk specimen deformed in plane simple shear. Thus, either *r*-slip or some other deformation mechanism has to compensate for this discrepancy. Since the results of the microstructural analysis suggest that the aspect ratio obtained by both methods (surface and grain volume) is too high, *r*-slip, i.e. an intragranular deformation mechanism, cannot be the only additional deformation mechanism, and the possibility of intergranular deformation mechanisms has to be investigated.

A behaviour where grain flattening lags behind the theoretical values while rotation is too fast, is to be expected for the deformation of stiff grains in a soft matrix. In an aggregate where grain-boundary sliding is occurring each grain acts as a stiff inclusion in a softer matrix: while the grain deforms by intracrystalline deformation mechanisms only, the bulk of the surrounding grains may additionally deform by grain boundary sliding. Hence, in terms of bulk deformation, the aggregate of grains as a whole acts as the softer material when compared to an individual grain.

We now consider CT 6 (700°C), which is deformed in the intracrystalline slip regime, the deviation of the axial ratio from the theoretical value is more pronounced than for the samples deformed in the twinning regime and indications of recrystallization along the grain boundaries can be observed (Fig. 8d). Within these mantle regions, slip between grains could be taken up. This implies another definition of the grain boundary. A more or less narrow zone around the grain boundary proper (i.e. the visually defined grain boundary) is interpreted as the mechanically effective grain boundary while the extent of the mechanically coherent grain is smaller than the volume enclosed by the visually defined grain boundary (see Fig. 28). 'Grain-boundary sliding' then means displacement of the coherent cores of grains past each other along the mechanically 'softer' grain-boundary zones. Within the mechanical grain-boundary zone the deformation of the visually defined grain boundary is determined by the governing deformation mechanism, i.e. the p–T regime. In the case of CT 6 (700°C), the grain boundary has been located somewhere within the rotation recrystallization zone. Similar

core mantle structures associated with rotation recrystallization have been observed in Al–5%Mg (Humphreys & Drury 1986).

But even at the lowest temperatures, the deformational behaviour of the calcite grains can be interpreted in terms of such a core–mantle structure where an increased amount of deformation in the mantle region leads to the patterns of surface orientation described above. In the twinning regime, where dynamic recrystallization is absent, it is more difficult to trace the exact nature of intergranular deformation. As an example, Fig. 8(b) reveals another kind of core–mantle microstructure. While the grain interior is completely twinned, the grain boundary area exhibits small triangular areas in an untwinned orientation. As a consequence, the strain due to *e*-twinning in the grain boundary will differ from that of the cores of the grains. It is also feasible that grain-boundary sliding or microshearing along grain boundaries will occur.

There is an important consequence to the above-mentioned strain partitioning between core and mantle of calcite grains: taking grain boundaries as passive markers of the deformation leads to erroneous strain estimates. The magnitude of shear is underestimated (since the axial ratio, b/a, is too high) and the inferred shear direction is a few degrees off (since the preferred orientation, α_p, is too low). However, the surface orientation in itself, being unimodal and having a symmetric characteristic shape, does not offer an indication for rotational vs irrotational strain (just as the strain ellipse in itself does not offer such an indication).

Results for Carrara marble from the intracrystalline slip to the grain-boundary migration regime

At temperatures of 700°C and above (CT 3, 700°C; CT 2, 800°C; CT 7, 800°C; and CT 4, 900°C) the surface orientation changes from symmetric unimodal (corresponding to an elliptical characteristic shape) to asymmetric bimodal (corresponding to a characteristic shape of the form of a lozenge). The transition is gradual, spanning a temperature range from 700 to 900°C, i.e. the change from the intracrystalline slip regime to the grain-boundary migration regime. The growing asymmetry can be observed in the projection diagrams (column (a), Fig. 24) where the angular difference, $\Delta\alpha$, between minimum and maximum length of projection decreases well below 85° (for symmetric characteristic shapes the difference should be 90°, a deviation of 5° is allowed for sampling errors). The growth of the second maximum is best seen in the rose diagrams (column (b), Fig. 24).

The first maximum of the preferred orientation of grain-boundary surface rotates into close parallelism with the shear-zone boundary while the second maximum is established at an orientation of about 70° inclined into the direction of shear. It is interesting to note that the transition of surface orientation from unimodal to bimodal is gradual. An analogous gradual transition of the crystallographic preferred orientation from the intracrystalline slip regime (CT 6, 700°C) to the grain-boundary migration regime (CT 7, 800°C, see Fig. 15) could not be demonstrated due to lack of sufficient data.

The orientation distribution of the long axes of grains does not reflect the asymmetry of the grain-boundary surface. The single maxima of the rose diagrams (column (e), Fig. 24) imply a preferred orientation of the long axes of the individual grains along a direction which deviates from the flattening plane towards the shear-zone boundary. Such an independent development of surface orientation and grain-volume orientation can remain undetected under coaxial conditions where a potential surface asymmetry is cancelled, for example, through overprinting of conjugate sets of shear zones. In Fig. 26 results are shown for Carrara marble which has been selected from a dextral shear zone within a coaxially deformed sample (sample 2685, deformed at 900°C, see Schmid *et al.*, 1980). The surface analysis shows the same asymmetric pattern as the corresponding shear experiment (CT 4). Note that the shear direction is inclined at about 30° clockwise with respect to the x-direction.

In the shear experiments, increasing temperature yields an increasing amount of horizontal and slightly clockwise inclined grain-boundary surface, which leads to the low angle first maximum, and there is an increasing fraction of grain boundary oriented at 70°, which leads to the second maximum of surface orientation (see evolution of rose diagrams from CT 3 (700°C) to CT 4 (900°C), column (b) in Fig. 24). The mechanisms by which these two orientations are effected are difficult to grasp. The generation of horizontal and subhorizontal grain-boundary surface may be attributed to shear along grain boundaries or mechanical grain-boundary zones, whereas the oblique orientation may be due to the formation of new grain boundaries along pre-existing subgrain boundaries.

At 800°C, the asymmetric characteristic shape is established already at small shear strains. As shearing progresses the lozenge shape is more pronounced and the axial ratio decreases slightly (compare column (c), Fig. 24, for CT 2 (800°C) where $\gamma \approx 1$ and CT 7 (800°C) where $\gamma \approx 3$). In other words, while it is possible to determine the *sense* of shear it is impossible to estimate the *magnitude* from the surface orientation. But in contrast to the low temperature samples, the surface orientation, through its asymmetry, yields an immediate criterion for rotational strain.

Another point worth noticing is the sensitivity of the surface analysis. In Fig. 21(b)–(d), the grain-boundary outlines of CT 3 (700°C), CT 2 (800°C) and CT 4 (900°C) are shown. The corresponding surface orientations are shown in Fig. 24. The bimodality of the surface orientation of CT 4 can be guessed by looking at the drawing of the grain boundaries. But in the case of CT 2 and CT 3 this is impossible. And since the grain-volume analysis indicates only one preferred orientation, any strain analysis based on the shape of grain volumes could not detect the irrotational nature of the strain.

Results for Solnhofen limestone in the intracrystalline slip regime and the grain-boundary sliding regime

In contrast to the evaluation of the Carrara marble samples, which uses all grain sizes, the analysis of Solnhofen limestone is restricted to the largest grain size (see Appendix 3 for discussion). The results are shown in Fig. 25. For an interpretation in terms of strain, a picture consistent with that of Carrara marble emerges. At low temperatures (i.e. in the intracrystalline slip regime), the surface orientation, being unimodal and symmetric, does not offer any direct indication for shear deformation. Moreover, analysis of grain-boundary surface and of grain volumes coincide. For ST 2 (500°C), the strain inferred from the surface and volume analysis corresponds, within measuring errors, to the applied shear strain. For ST 1 (700°C), the characteristic shape is still asymmetric, the orientation of the long axis is correct; however, the high axial ratio, b/a, indicates too little flattening. This situation seems similar to the out of plane deformation by *e*-twinning of Carrara marble. But Solnhofen limestone does not twin at these temperatures, therefore a small-scale grain-boundary mobility is inferred which accounts for the high b/a values.

With increasing temperature (i.e. in the grain-boundary sliding regime) the deviation from the symmetric surface orientation increases (ST 5, 700°C) until an asymmetric characteristic shape is obtained. For ST 4 (800°C), a bimodal surface orientation distribution is established with a subhorizontal first maximum and a second maximum at 70°. This indicates grain-boundary migration and supports the idea that grain-boundary sliding and grain-boundary migration go hand-in-hand in the case of Solnhofen limestone. The axial ratio determined from the projection diagrams, $A(\alpha)$ or $B(\alpha)$, is even higher than that for Carrara marble (CT 4, 900°C) and consequently the characteristic shape is more isometric. As was shown for the Carrara marble sample (CT 4, 900°C) the surface orientation, by its bimodality, and the characteristic shape, by its asymmetry, indicate that the strain is rotational. And again, the direction of shear but not its magnitude can be determined. Note again the sensitivity of the surface analysis which detects the bimodal surface orientation distribution although it is almost invisible on Fig. 21(f).

Comparison of results for Carrara marble and Solnhofen limestone

At the lower temperatures, Carrara marble samples deformed in the twinning and the intracrystalline slip regime; for the Solnhofen limestone only the intracrystalline slip regime was observed. In both cases, the surface orientation yields an ellipse as the characteristic shape. For Carrara marble this ellipse has an axial ratio, b/a, which is too high and a preferred orientation, α_p, which is too low. This fabric development can be attributed to the formation of core–mantle structures. For Solnhofen limestone, at first, the fabric ellipse more or less coincides with the theoretical strain ellipse. Deviations of the axial ratio, b/a, have to be attributed to grain-boundary migration.

Going to higher temperatures, there is a gradual transition from the surface orientation typical for the intracrystalline slip regime to that typical for the grain-boundary migration regime (in the case of Carrara marble) or the grain-boundary sliding regime (in the case of Solnhofen limestone). At the highest temperatures the surface orientations of Carrara marble and Solnhofen limestone are essentially the same: they show asymmetric surface distributions which can be attributed to grain-boundary migration. In both cases, the surface orientation yields a criterion for rotational strain and for the shear direction.

Shape analysis shows that, at high temperatures, the visually defined grain boundaries of Carrara marble change from smooth to serrated, while the opposite is true for Solnhofen limestone. However, in both cases the characteristic shape is more isometric than at the lower temperatures, although, at high temperature, the individual grains of Carrara marble are very complicated three-dimensional networks (Fig. 8f) whereas those of Solnhofen appear like compact, simply connected grains (Fig. 8h).

GEOLOGICAL APPLICATIONS

The results of this study are relevant for geological problems in two respects: (1) the experiments are helpful for interpreting the microfabric of sheared calcite tectonites in particular; and (2) the results of the experiments with calcite have implications for interpreting the microfabric of sheared rocks in general.

Applications to naturally deformed calcite rocks

Pole figures with the *c*-axis maximum deflected from the normal to the foliation in a direction towards the position of σ_1 (i.e. a deflection opposite to the imposed sense of shear) have frequently been observed in naturally deformed calcite rocks (Schmid *et al.* 1981, Dietrich & Song 1984). This texture pattern corresponds to the texture observed in the twinning regime. Since twinning rapidly reorients the *c*-axis into a direction close to the position of σ_1, these *c*-axis maxima are expected to provide a good approximation of the direction of σ_1 during the closing stages of deformation. Dietrich & Song (1984) observed a very remarkable parallelism of the directions of these *c*-axis maxima with respect to geographical co-ordinates over a wide area in the root zone of the Helvetic Nappes of Western Switzerland. This observation suggests that the texture of these rocks reflects the stress field which must have been fairly homogeneous over a wide area during the closing stages of ductile deformation. Figure 29 pictures a small-scale fold from the Eastern Helvetic Nappes (Pfiffner 1978). The asymmetric pattern of the pole figures with respect to the axial plane of the fold remains constant all around the fold. This small-scale example again illustrates that

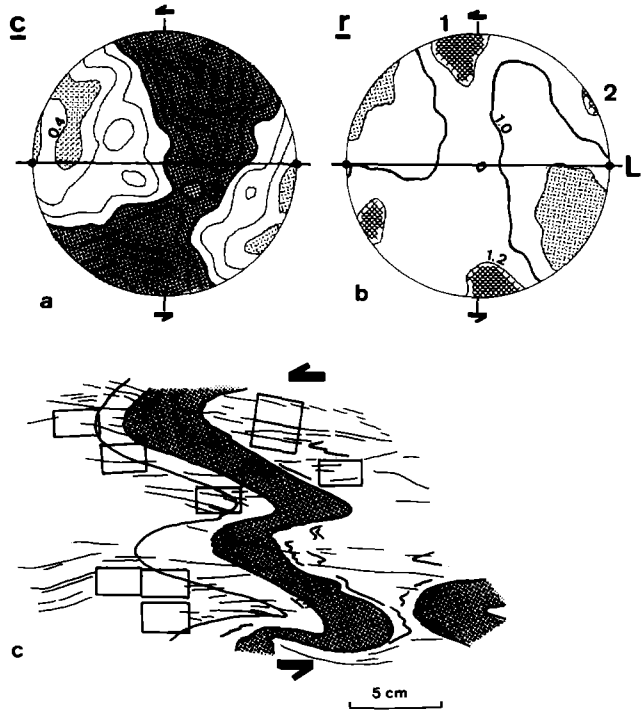

Fig. 29. Pole figures for the *c*-axes (a), and the poles to the *r*-planes (b) of a natural calcite tectonite. Note the remarkable similarity with the pole figures of experimental samples depicted in Fig. 10(d) & (g). Specimen taken from a small-scale fold in the Helvetic nappes of Switzerland (Calanda nappe, Pfiffner 1978). The pole figures were calculated from the ODF. (a) *c*-axis pole figure. Contour intervals 0.2 of a uniform distribution. Shaded area with a density >1.0 of a uniform distribution. Horizontal line: trace of the foliation which is parallel to the axial plane of the fold. (b) Pole figure for the *r*-poles. Contour intervals 0.2 of a uniform distribution. L marks the stretching lineation oriented NW–SE. Horizontal line: trace of the foliation. Maxima labelled 1 and 2 correspond to the maxima labelled with the same numbers in Fig. 10(g). (c) Sketch of the small-scale fold from which specimens were taken at the localities indicated by the rectangles. All the specimens were measured and found to be identical with the texture depicted in Fig. 26 (a) & (b) with respect to the foliation as a reference line. Shaded layer: marly limestone.

the texture was acquired during the closing stages of the folding process, when the passive fold suffered a homogeneous shearing overprint.

The textures characteristic of the twinning regime are typically observed at temperatures slightly below or within lower-greenschist facies conditions. The microstructure of these tectonites is often characterized by extensive twinning (Schmid 1982a). However, in many other cases, as in the limestone depicted in Fig. 29, no twinning at all can be observed. In view of the strong flattening of individual grains the microstructure would indicate deformation within the intracrystalline slip regime. In spite of the frequent absence of visible twins, the distinctly different textures corresponding to the intracrystalline slip regime have so far never been measured in naturally deformed calcite rocks. Thus, in many cases the measured texture is indicative of twinning whereas the microstructure would indicate intracrystalline slip.

This apparent contradiction may be solved with the help of some microstructural observations made in specimen CT 5. Frequently more than 90% of the grain volume is in a twinned orientation (Fig. 9) and only small triangular regions with the orientation of the host grain are preserved in the grain-boundary region (Fig. 8b). In nature, deformation events are often followed by thermal adjustments which lead to an increase in temperature under static conditions (e.g. in the footwall of an overthrust). In fact, Pfiffner (1982) provided independent evidence for such a thermal adjustment in the area where the small-scale fold depicted in Fig. 29 was collected. Since calcite is known to be very susceptible to annealing, twin-boundary migration may completely eliminate domains in the orientation of the host grain and hence eliminate all the visible traces of twinning. Twin-boundary migration has been observed at elevated temperatures in coaxially deformed Carrara marble (Schmid *et al.* 1980) and in nature (Groshong *et al.* 1984, Schmid *et al.* 1981). In conclusion, the texture still preserves the features diagnostic for the deformation mechanism while the microstructure may lead to erroneous interpretations.

Schmid *et al.* (1981) and Schmid (1982a) documented the complete absence of a crystallographic preferred orientation in fine-grained calcite mylonites which were interpreted to have deformed by grain-boundary sliding. In the present experiments, however, specimens deformed in the grain-boundary sliding regime develop a texture, although distinctly weaker in comparison with specimens deformed in the intracrystalline slip regime. The total absence of texture in the natural calcite mylonites may be due to their smaller grain size, which would further supress the contribution of intracrystalline slip to the total rock strain. The change in deformation mechanism from intracrystalline slip towards grain-boundary sliding observed during progressive myloniti-

zation of limestones was predicted to lead to strain softening due to the grain size reduction by rotation recrystallization (Schmid 1982b). In one of the highly strained Carrara marble specimens (CT 6, see Fig. 8c & d) the volume of fine-grained material produced by rotation recrystallization was either too small to produce significant work softening (Fig. 5 indicates very minor amounts of work softening for CT 6) or, alternatively, the grain size produced was still too large to induce a change in deformation mechanism towards grain-boundary sliding. However, local strain concentrations along incipient *C*-planes containing large amounts of recrystallized material are clearly visible in Fig. 8(c). This suggests that significant work softening due to grain size reduction might be expected at shear strains in excess of $\gamma = 3$.

It was mentioned earlier that natural equivalents of the textures diagnostic for the intracrystalline slip regime have not yet been found. The same holds for textures diagnostic for the grain-boundary migration regime, where basal slip was inferred to be the dominant slip system. The reasons for this may well lie in the extreme readiness of calcite to undergo annealing. At metamorphic conditions higher than lower-greenschist facies, where both these microfabric regimes are expected to have existed, annealing could completely overprint the microstructure and texture. A good example for this is found in the marble quarries of Carrara (Italy) where no visible traces of deformation are seen in the microfabric in spite of the ample evidence for isoclinal folding. If high grade marbles do exhibit a texture (e.g. Yule marble) it may well have formed during the closing stages of deformation at lower temperatures.

Applications to sheared rocks in general

Both in the intracrystalline slip regime and the grain-boundary migration regime, progressive simple shear eventually establishes an end orientation for easy slip with respect to the dominant slip systems. During the initial stages of simple shear both synthetic and antithetic slip occur. As a consequence of this the synthetically operating slip system is not exactly aligned with the shear-zone boundary but is systematically deflected towards the plane of finite flattening (Fig. 14b & d). With progressive deformation the slip systems oriented for synthetic slip rotate into strict parallelism with the shear zone boundary (Fig. 15c & e). Identical observations have been made in torsion experiments on ice (Bouchez & Duval 1982) and there is a remarkable agreement with the predictions of Etchecopar (1977).

In terms of quartz *c*-axis pole figures, these observations suggest that crossed girdles with one dominating girdle perpendicular to the shear zone boundary (analoguous to the *c*-axis pattern observed in CT 7, see Fig. 15f) are expected at low shear strains during simple shear. With progressive simple shear a single girdle, oriented perpendicular to the shear-zone boundary, will develop. Thus, ideally, single girdles should not only indicate the sense of shear but also the magnitude of shear strain. Schmid & Casey (1986) found such a configuration in small-scale shear zones. Within mylonite belts, however, the amount of shear strain, indicated by the angle of inclination of the *c*-axis girdle with respect to the foliation, has been found to be systematically too small by a great number of workers (e.g. Mancktelow 1987). The reasons for this finding remain unclear.

The exact nature of the mechanisms of lattice reorientation leading to an end orientation for easy slip in the absence of migration recrystallization are still unknown. However, when extensive migration recrystallization is present, the observations on specimen CT 7 (grain boundary migration regime, Fig. 8e & f) strongly support a model proposed by Schmid & Casey (1986): preferential elimination of grains which are unfavourably oriented for easy slip, enhancing the process of lattice reorientation. As a consequence of this, work softening occurred, as seen in Fig. 5 (CT 7 and CT 4). This mechanism of work softening (geometric softening) is different from that discussed earlier (softening induced by a change in deformation mechanism due to grain size reduction). The experiments indicate that geometric softening occurs very rapidly during progressive simple shear provided that grain boundary migration assists rapid lattice reorientation.

The quantitative microstructural analysis demonstrated that even in the absence of recrystallization, grain shape does not always reflect finite strain. It was observed that often the aspect ratio of the grains indicates too small a strain and that the orientation of the long axis was too close to the shear-zone boundary. Such a behaviour would be expected for a more viscous strain marker embedded in a matrix of lower viscosity (Ghosh & Ramberg 1976). In analogy to the inclusion-matrix problem an individual mineral grain may be considered as an inclusion within a matrix consisting of other mineral grains and, additionally, grain boundaries or grain-boundary regions. If the grain boundary as such accommodates translations of grains with respect to each other (grain-boundary sliding), or if the grain-boundary region accounts for translations of the cores of the grains due to a lower viscosity in the mantle region (core–mantle structures), an individual grain is expected to be effectively stronger than the surrounding matrix.

The reliability of the following important shear sense indicator frequently found in quartz under higher metamorphic grade was confirmed by the quantitative microstructural analysis: the preferred grain-boundary alignment along two planes, the dominant being parallel, the other at a high angle, to the shear-zone boundary (Lister & Snoke 1984). The nature of the mechanism which leads to this grain-boundary preferred orientation remains unclear. The oblique orientation is possibly controlled by pre-existing subgrain boundaries and deformation bands, while the dominant alignment parallel to the shear-zone boundary may be caused by microshears along groups of grains in that direction.

Acknowledgements—The experiments have been performed while one of us (S. Schmid) was a visitor at the Center for Tectonophysics,

Texas A & M University with financial support from the Landis & Gyr Stiftung, Zug, Switzerland. R. Fletcher, J. Logan, M. Friedman and all their collegues at the Center have been very helpful, and their hospitality made the visit a profitable one. We thank M. Casey for providing the texture analysis programs. G. Lister, A. Pfiffner, M. S. Paterson, an anonymous reviewer, and in particular, Jan Tullis, helped to improve the original manuscript. The work on quantitative microstructural analysis was supported by the Schweizerische Nationalfonds (Projekt 2.162-0.83). We wish to thank R. Gschwind at the Department of Scientific Photography, Basel, for use of digitizing equipment and computer facilities.

REFERENCES

Ashby, M. F. & Verrall, R. A. 1973. Diffusion—accommodated flow and superplasticity. *Acta metall.* **21**, 149–163.

Bouchez, J. L. & Duval, P. 1982. The fabric of polycrystalline ice deformed in simple shear: experiments in torsion, natural deformation and geometrical interpretation. *Textures Microstruct.* **5**, 171–190.

Bunge, H. J. 1969. *Mathematische Methoden der Texturanalyse.* Akademie Verlag, Berlin.

Casey, M. 1981. Numerical analysis of X-ray texture data: an implementation in Fortran allowing triclinic or axial specimen symmetry and most crystal symmetries. *Tectonophysics* **78**, 51–64.

Casey, M., Rutter, E. H., Schmid, S. M., Siddans, A. W. B. & Whalley, J. S. 1978. Texture development in experimentally deformed calcite rocks. In: *Proc. ICOTOM 5* (Edited by Gottstein, G. & Lucke, K.) March 1978, Aachen **2**, 231–240.

Dietrich, D. & Song, H. 1984. Calcite fabrics in a natural shear environment, the Helvetic nappes of western Switzerland. *J. Struct. Geol.* **6**, 19–32.

Etchecopar, A. 1977. A plane kinematic model of progressive deformation in a polycrystalline aggregate. *Tectonophysics* **39**, 121–139.

Friedman, M., Handin, J., Higgs, N. C. & Lantz, J. R. 1979. Strength and ductility of four dry igneous rocks at low temperatures to partial melting. In: *Proceedings of the 20th U.S. Symposium on Rock Mechanics*, Austin, Texas, 35–50.

Friedman, M. & Higgs, N. C. 1981. Calcite fabrics in experimental shear zones. *Am. geophys. Un. Geophys. Monogr.* **24**, 11–27.

Ghosh, S. K. & Ramberg, H. 1976. Reorientation of inclusions by combination of pure shear and simple shear. *Tectonophysics* **34**, 1–70.

Groshong, R. H. 1972. Strain calculated from twinning in calcite. *Bull. geol. Soc. Am.* **83**, 2025–2038.

Groshong, R. H., Pfiffner, O. A. & Pringle, L. R. 1984. Strain partitioning in the Helvetic thrust belt of Eastern Switzerland from the leading edge to the internal zone. *J. Struct. Geol.* **4**, 429–442.

Guillope, M. & Poirier, J. P. 1979. Dynamic recrystallization during creep of single-crystalline halite: an experimental study. *J. geophys. Res.* **84**, 5557–5567.

Humphreys, F. J. & Drury, M. R. 1986. The formation of high angle grain boundaries and new grains during the deformation of Al–5%Mg at elevated temperatures. *Aluminium Technology '86* The Institute of Metals, London. Abstract Volume, Book 3, 76.1–76.6.

Hobbs, B. E. 1968. Recrystallization of single crystals of quartz. *Tectonophysics* **6**, 353–401.

Kern, H. & Wenk, H. R. 1983. Calcite texture development in experimentally induced ductile shear zones. *Contr. Miner. Petrol.* **83**, 231–236.

Lister, G. S. 1978. Texture transitions in plastically deformed calcite rocks. In: *Proc. 5th Int. Conf. on Textures of Materials.* Springer Verlag, Berlin, 199–200.

Lister, G. S. & Snoke, A. W. 1984. *S–C* Mylonites. *J. Struct. Geol.* **6**, 617–638.

Mancktelow, N. S., 1987. Quartz textures from the Simplon fault zone, SW Switzerland and N Italy. *Tectonophysics* **135**, 133–153.

Nadai, A. 1963. *Theory of Flow and Fracture of Solids.* McGraw-Hill, New York.

Nye, J. F. 1953. The mechanics of glacier flow. *J. Glaciol.* **2**, 82–93.

Panozzo, R. 1983. Two-dimensional analysis of shape fabric using projections of lines in a plane. *Tectonophysics* **95**, 279–294.

Panozzo, R. 1984. Two-dimensional strain from the orientation of lines in a plane. *J. Struct. Geol.* **6**, 215–221.

Panozzo, R., 1986. Quantitative description of connected and unconnected surfaces in rocks. In: *Fragmentation, Form and Flow in Fractured Media. Ann. Israel Phys. Soc.* **8**, 19–41.

Panozzo, R. & Hürlimann, H. 1983. A simple method for the quantitative discrimination of convex and convex–concave lines. *Microscopica Acta* **87**, 169–176.

Paterson, M. S. 1979. Deformation mechanics in carbonate crystals. In: *Physics of Materials* (edited by Borland, D. W., Clarebrough, L. M., Moore, A. J. W.). CSIRO and Dept. Metallurgy, University of Melbourne, 109–208.

Pfiffner, O. A. 1978. Der Falten- und Kleindeckenbau im Infrahelvetikum der Ostschweiz. *Eclog. geol. Helv.* **71**, 61–84.

Pfiffner, O. A. 1982. Deformation mechanisms and flow regimes in limestones from the Helvetic Zone of the Swiss Alps. *J. Struct. Geol.* **4**, 429–442.

Rutter, E. H. 1970. An experimental study of the factors affecting the rheological properties of rocks in simulated geological environments. Unpublished Ph.D. thesis, Imperial College, London.

Rutter, E. H. 1974. The influence of temperature, strain rate and interstitial water in the experimental deformation of calcite rocks. *Tectonophysics* **22**, 311–334.

Rutter, E. H. & Rusbridge, H. 1977. The effect of non-coaxial strain paths on crystallographic preferred orientation development in the experimental deformation of a marble. *Tectonophysics* **39**, 73–86.

Schmid, S. M. 1975. The Glarus Overthrust: field evidence and mechanical model. *Eclog. geol. Helv.* **68**, 247–280.

Schmid, S. M. 1982a. Laboratory experiments on rheology and deformation mechanisms in calcite rocks and their application to studies in the field. Habilitationsschrift E.T.H. Zürich. *Mitt. geol. Inst. E.T.H. u. Univ. Zürich, N.F.* **241**, 1–106.

Schmid, S. M. 1982b. Microfabric studies as indicators of deformation mechanisms and flow laws operative in mountain building. In: *Mountain Building Processes* (edited by Hsu, K. J.). Academic Press, London, 95–110.

Schmid, S. M., Boland, J. N. & Paterson, M. S. 1977. Superplastic flow in finegrained limestone. *Tectonophysics* **43**, 257–291.

Schmid, S. M., Paterson, M. S. & Boland, J. N. 1980. High temperature flow and dynamic recrystallization in Carrara marble. *Tectonophysics* **65**, 245–280.

Schmid, S. M., Casey, M. & Starkey, J. 1981. The microfabric of calcite tectonites from the Helvetic nappes (Swiss Alps). In: *Thrust and Nappe Tectonics* (edited by McClay, K. R. & Price, N. J.). *Spec. Publs geol. Soc. Lond.* **9**, 151–158.

Schmid, S. M. & Casey, M. 1986. Complete fabric analysis of some commonly observed quartz *c*-axis patterns. *Am. geophys. Un., Geophys. Monogr.* **36**, 263–268.

Spang, J. H. 1974. Numerical dynamic analysis of calcite twin lamellae in the Greenport Center syncline. *Am. J. Sci.* **274**, 1044–1058.

Spiers, C. J. 1979. Fabric development in calcite polycrystals deformed at 400°C. *Bull. Minéral.* **102**, 282–289.

Turner, F. J. 1953. Nature and dynamic interpretation of deformation lamellae in calcite of three marbles. *Am. J. Sci.* **251**, 276–298.

Turner, F. J., Griggs, D. T. & Heard, H. 1954. Experimental deformation of calcite crystals. *Bull. Geol. Soc. Am.* **65**, 883–934.

Turner, F. J. & Weiss, L. E. 1963. *Structural Analysis of Metamorphic Tectonites.* McGraw-Hill, New York.

Turner, F. J. & Orozco, M. 1976. Crystal bending in metamorphic calcite, and its relation to associated twinning. *Contr. Miner. Petrol.* **57**, 83–97.

Wenk, H. R., Kern, H., VanHoutte, P. & Wagner, F. 1986. Heterogeneous strain in axial deformation of limestone, textural evidence. *Am. geophys. Un., Geophys. Monogr.* **36**, 287–295.

Wenk, H. R., Venkitasubramanyan, C. S. & Baker, D. W. 1973. Preferred orientation in experimentally deformed limestone. *Contr. Miner. Petrol.* **38**, 81–114.

APPENDIX 1

Method of converting flow laws obtained in pure shear testing into simple shear

The second invariant of the deviatoric stress tensor can be expressed as:

$$J_2 = 1/2\ (s_1^2 + s_2^2 + s_3^2),$$

where $s_{1,2,3}$ are the principal deviatoric stresses.

In a pure shear experiment at the confining pressure p the total stress tensor is the sum of the deviatoric stress tensor and the lithostatic pressure:

$$\begin{vmatrix} p+\Delta\sigma & 0 & 0 \\ 0 & p & 0 \\ 0 & 0 & p \end{vmatrix} = \begin{vmatrix} 2/3\Delta\sigma & 0 & 0 \\ 0 & -1/3\Delta\sigma & 0 \\ 0 & 0 & -1/3\Delta\sigma \end{vmatrix} + \begin{vmatrix} p+1/3\Delta\sigma & 0 & 0 \\ 0 & p+1/3\Delta\sigma & 0 \\ 0 & 0 & p+1/3\Delta\sigma \end{vmatrix}$$

and, consequently, the second invariant of the deviatoric stress tensor in coaxial testing can be calculated to be $J_2 = 1/3\,(\Delta\sigma)^2$.

Similarly, we can write for simple shearing

$$\begin{vmatrix} p+s_1 & 0 & 0 \\ 0 & p & 0 \\ 0 & 0 & p-s_1 \end{vmatrix} = \begin{vmatrix} s_1 & 0 & 0 \\ 0 & 0 & 0 \\ 0 & 0 & -s_1 \end{vmatrix} + \begin{vmatrix} p & 0 & 0 \\ 0 & p & 0 \\ 0 & 0 & p \end{vmatrix}$$

and, the second invariant of the deviatoric stress tensor in simple shear can be written as $J_2 = s_1^2$.

In simple shear the value of s_1 is better expressed in terms of the shear stress τ_{xy} acting along the shear-zone boundary. Because τ_{xy} is the maximum shear stress we can write:

$$\tau_{xy} = (\sigma_1 - \sigma_2)/2 \text{ and } J_2 = \tau_{xy}^2.$$

Now, we can generalize the flow laws for equations (1) and (2) into:

$$e_{ij} = \frac{\sqrt{3}}{2}\sqrt{\frac{1}{J_2}}\,A \exp(B\sqrt{3J_2})\,\sigma_{ij} \qquad \text{(A1)}$$

and

$$e_{ij} = \frac{(3^{1/2})^{n+1}}{2} B\,(\sqrt{J_2})^{n-1}\sigma_{ij} \qquad \text{(A2)}$$

such that equations (A1) and (A2) reduce to equations (1) and (2), respectively, for the special case of coaxial flattening.

In simple shear, the flow law can now be expressed in terms of the constants A, B, C and n derived by coaxial pure shear experiments [equations (3) and (4) see text].

APPENDIX 2

Methods of fabric analysis and strain interpretation

(a) *Surface fabric and grain-volume fabric.* Two types of fabric analysis are carried out, which involve digitization of grain-boundary outlines on enlarged photographs and evaluation by computer programs described elsewhere (Panozzo 1984). Digitizing equipment and computer facilities of the Institute of Physical Chemistry in Basel were used. The input for the computer programs consists of the digitized x–y co-ordinate points which are sampled along the grain-boundary outlines. In order to avoid distortions of the orientation data (Panozzo 1986), the original grain boundaries are reconstructed from these points by two-dimensional splining. On these reconstructed outlines, equally spaced points are used to define a set of short straight line segments for each grain boundary. Since this is done on two-dimensional sections, analysis of surface orientation considers linear traces (Fig. A1a), and analysis of the individual grain volumes considers their cross-sectional areas (Fig. A1b).

For the linear segments and for the long axes of the cross-sectional areas, the two-dimensional orientation distribution functions, $h(\alpha_i)$, are obtained (Fig. A1). Furthermore, the linear segments and the cross-sectional areas are projected onto a reference axis, x, while rotating through an angle of 180°.

In surface evaluation, the rose diagrams represent the total length of grain-boundary outline per angle of orientation. The projection diagrams, $A(\alpha)$, represent the total length of projected grain-boundary

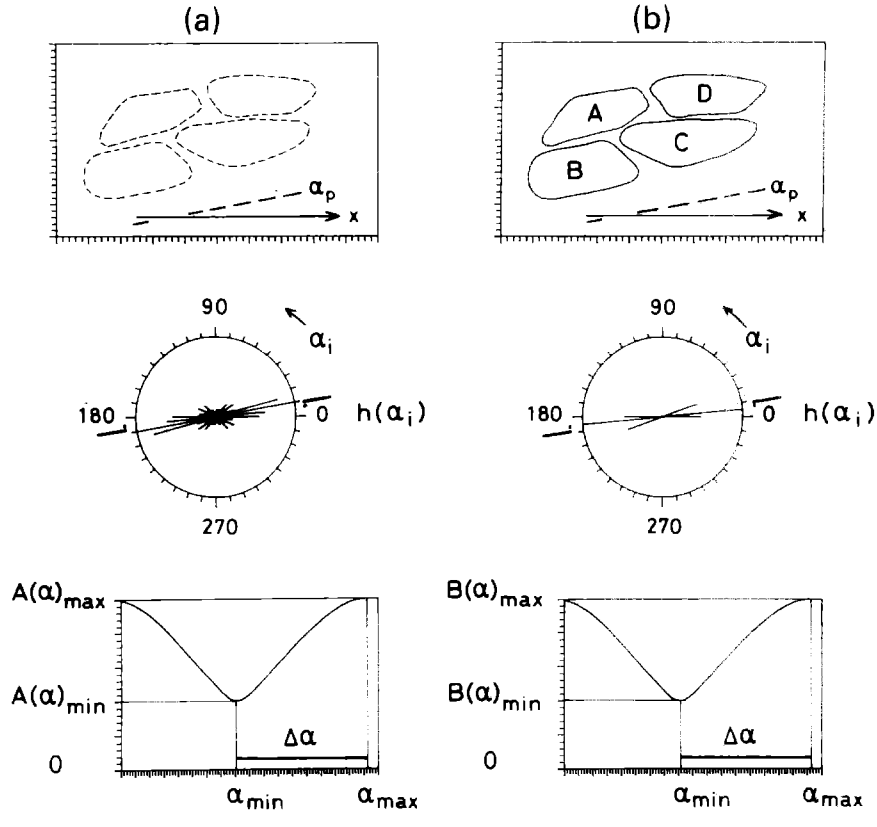

Fig. A1. Illustration of the significance of results obtained from surface analysis (a), and grain-volume analysis (b). *Top*: In the digitizing procedure, approx. 100 straight line segments are used (a), to approximate the outlines of the grains (A, B, C, D) (b). α_p = preferred orientation of fabric with respect to reference direction x. *Middle*: rose diagrams representing the orientation distribution function, $h(\alpha_i)$, of line segments (a), and particle long axes (b). α_i is counterclockwise; the bar indicates α_p derived from α_{min}; the point indicates α_p derived from α_{max}. *Bottom*: projection diagrams: $A(\alpha)$ = total length of projection of line segments; $B(\alpha)$ = total length of projection of particle shapes. Diagrams are scaled such that $A(\alpha)_{max} = 1.00$ and $B(\alpha)_{max} = 1.00$. Therefore, the value of the axial ratio of the fabric ellipse: $b/a = A(\alpha)_{min}$ or $b/a = B(\alpha)_{min}$. The angles where the projection function reaches minimum and maximum values are α_{min} and α_{max}, respectively. The difference, $\Delta\alpha = \alpha_{max} - \alpha_{min}$, is 90° if the characteristic shape is mirror symmetric. The preferred orientation of the fabric is $\alpha_p = 90° - \alpha_{min}$ or $\alpha_p = 180° - \alpha_{max}$.

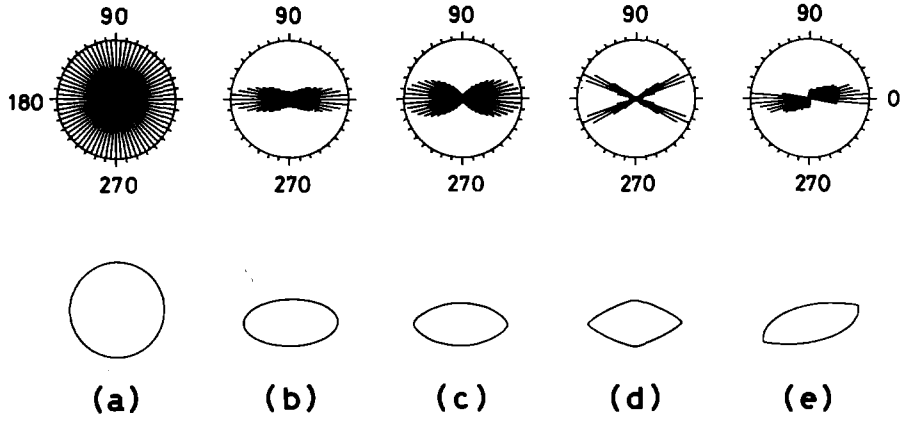

Fig. A2. Examples of characteristic shapes of line fabrics. *Top*: rose diagrams of orientation distribution function, $h(\alpha_i)$. *Bottom*: characteristic shape. The following distribution functions are shown: (a) uniform distribution (of random orientation of lines or circle); (b) unimodal, symmetric distribution (of strained random orientation of lines or strain ellipse); (c) normal distribution, (= unimodal symmetric); (d) bimodal symmetric distribution; (e) unimodal asymmetric distribution.

outline onto the x-axis per angle of rotation. In the case of grain-volume evaluation, the rose diagrams represent the total length of grain axes per angle of orientation and the projection diagrams, $B(\alpha)$, represent the total length of projected cross-sectional areas onto the x-axis per angle of rotation. If the grain-boundary outlines are fully convex the projection diagrams $B(\alpha)$ and $A(\alpha)$ have to coincide (Panozzo 1984). Differences between the projection diagrams $A(\alpha)$ and $B(\alpha)$ may serve as indicators of surface convexity/concavity (Panozzo & Hürlimann 1983).

(b) *Definition of the characteristic shape.* The projection function, $A(\alpha)$, of any surface fabric is identical to the projection function of its characteristic shape. The characteristic shape of a fabric is obtained by linking the line segments by which the fabric is approximated (through the digitizing procedure) in the order of increasing slope (see Fig. A2). For a set of randomly oriented lines, this procedure yields a circle. The characteristic shape of a deformed set of lines is the strain ellipse (provided the lines were initially randomly oriented and can serve as passive markers of the deformation). Since the characteristic shape of any set of lines is always fully convex, the projection function of the characteristic shape and that of the corresponding set of line segments are identical (see Panozzo 1984).

(c) *Strain considerations.* In cases where the characteristic shape of a fabric is an ellipse, the projection diagrams are used to derive the axial ratio and the orientation of the long axis of the two-dimensional strain ellipse, the implicit assumption being that the undeformed state is characterized by random orientation of surface and that the present preferred orientation of the surface elements is due to deformation only.

The orientation distribution function of a circle is a constant, the corresponding rose diagram is shown in Fig. A2(a). The surface rose diagram of an ellipse is shown in Fig. A2(b). Note, that it is not equivalent to the normal distribution (Fig. A2c) which is useful for the description of particle alignment (Panozzo 1983). A set of lines which displays one or more preferred orientations may have any characteristic shape (cf. Fig. A2c–e). In order for the characteristic shape of a fabric to be an ellipse the rose diagram has to be unimodal and symmetric. Also, the curve of the projection diagram has to follow the projection function of an ellipse, which is the mathematical equivalent of the equation for the quadratic elongations of the strain ellipse. In the projection diagram of an ellipse, the minimum and maximum value occur at angles that are 90° apart, and the ratio obtained by dividing minimum by maximum value is the axial ratio of the ellipse.

$$b/a = A(\alpha)_{min}/A(\alpha)_{max} \text{ or } B(\alpha)_{min}/B(\alpha)_{max}$$
$$\alpha_p = 90° - \alpha_{min} \quad \text{or } 180° - \alpha_{max}.$$

The axial ratio and the orientation of the characteristic shape are best determined from the projection diagram because, contrary to the plot of the characteristic shape, it yields the result in numerical form.

(d) *Definition of long axes of grains.* In the present application, it was assumed that the longest projection of a grain represents twice its long axis, and that the projection at 90° from the longest one represents twice its short axis. In terms of the projection function, $B(\alpha)$, this choice is irrelevant. It only has an influence on the rose diagrams of long axes of grains where the total length of long axes are plotted against angle of orientation. For the surface fabric the problem of defining the axial ratio of individual grains involves less ambiguity than for grain-volume analysis.

APPENDIX 3

The initial state and homogeneity of samples

The characteristic shape of the starting material of Carrara marble is not a circle, i.e. an initial, anisotropic fabric is present. The fabric has been analysed at various sites on the thin section, and a considerable variation has been observed. The axial ratio of the characteristic shape, which is not an ellipse, may be as low as 0.80. In order to be sure that the discrepancy between the preferred orientation of the low temperature samples of Carrara marble and the theoretical values of the strain ellipse (see above) is not simply due to this initial (pre-strain) fabric the theoretical values for the shear deformation of ellipses was calculated. In Fig. 27, the measured values of b/a and α_p of the low temperature samples are plotted together with the theoretical curves for the two extreme cases (b/a = 0.80, and α_i = 43 or 73°, according to the possible orientations of the initial fabric with respect to the shear zone). It is clear that the measured values plot outside the variation that might be admitted on the basis of having an initial preferred orientation of surface. Therefore the deviation has been assumed to be real.

The orientation distribution function of the surface of the undeformed sample is asymmetric. It might be suspected that this asymmetry is conserved through the shear deformation and thus accounts for the resulting asymmetric orientation distributions of the higher temperatures samples. Synthetic shear deformation of the fabric of CT 012 (i.e. numerical transformation of the digitized outlines of the initial fabric) shows that the transformation obliterates the initial asymmetry (Fig. A3). Therefore, the deviation from symmetry of the deformed samples cannot be accounted for by the initial asymmetry. Also, from inspection of the low shear samples ($\gamma < 1.00$) it appears that the typical orientation distribution functions are established almost instantly, at the beginning of deformation, being more sensitive to the deformation regime than to the initial fabric.

The grain size of Carrara marble and Solnhofen limestone are almost two orders of magnitude apart (typical grain size for Carrara marble is 0.2 mm, for Solnhofen it is 4 μm). Accordingly, fabric analyses were carried out at different magnifications. For Carrara marble a magnification of 67 was used, for Solnhofen limestone the magnification was 1050. As a consequence, the areas of analysis of the Carrara samples (typically 3 × 3 mm) cover the entire width of the experimental shear zone, whereas those of the Solnhofen limestone

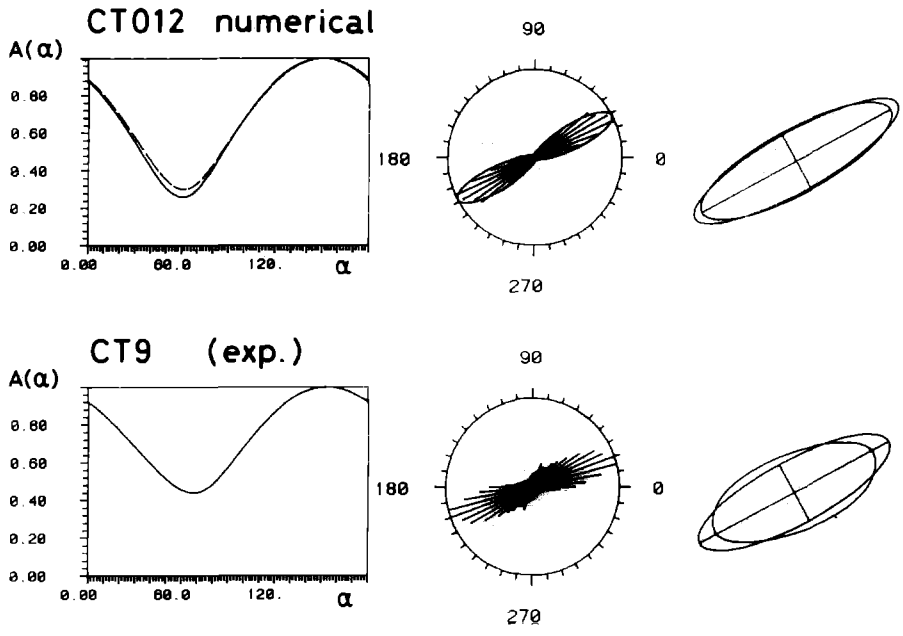

Fig. A3. Numerical deformation of undeformed sample CT 012 (top) vs experimental deformation of CT 9 (350°C) (bottom). In both cases, $\gamma = 1.27$. Dashed line and superposed line in rose diagram of CT 012 = theoretical strain ellipse.

($15 \times 25\,\mu m$) could cover only a small fraction of it; the area used was always taken from the center portion.

Inspection of samples of both rock types shows that with increasing temperatures and strain zones of higher and lower intensity of deformation are developed in the shear zones. At first, a zone of higher intensity forms along a plane that connects the two leading edges of the forcing blocks, later on, these zones grow parallel to the shear zone boundaries.

In the Solnhofen limestone the fabric appears heterogeneous; in particular, the area of homogenization seems to be greater than the area of analysis in those samples. This causes minor variations of the results from one area of analysis to the next (see Table A1).

A last difference between the quality of the primary data of the Carrara marble and that of the Solnhofen limestone arises from the selection of grains. On a given area of Carrara marble, all grains could be used. In contrast, the grain size of Solnhofen limestone is so small that only the largest fraction of particles could be used for the analysis.

Therefore, if the results obtained from the analysis of Carrara marble and those of Solnhofen limestone are to be compared one has to pay attention to the following points: (a) the averaging effect of using large areas of analysis for Carrara marble; (b) the variations between samples of Solnhofen limestone; and (c) the possibility of strain partitioning between large and small particles for Solnhofen limestone. As it has been impossible to monitor these influences, their possible effects have been neglected throughout the paper.

Table A1. Variation of axial ratios, b/a (= short axis/long axis), and angle of preferred orientation, α_p (Solnhofen limestone)

Sample	Average b/a	$\Delta(b/a)$	Average α_p(°)	$\Delta(\alpha_p)$(°)
ST 2	0.36	0.04	31	0
ST 1	0.57	0.08	33	6
ST 5	0.69	0.02	28	8
ST 4	0.85	0.01	28	2

$\Delta(\alpha_p)$ = difference of α_p between two measured values.
$\Delta(b/a)$ = difference of b/a between two measured values.